Received: 10 April 2023 | Revised: 14 March 2024 | Accepted: 24 March 2024

DOI: 10.1002/esp.5841

RESEARCH ARTICLE

ESPL WILEY

Observations and computational multi-phase modelling in tropical river settings show complex channel changes downstream from rainfall-triggered landslides

Diego Panici[1,2] | Georgina L. Bennett[2] | Richard J. Boothroyd[3,4] | Clàudia Abancó[2,5] | Richard D. Williams[3] | Fibor Tan[6] | Mark Matera[6]

[1]Centre for Resilience in Environment, Water and Waste (CREWW), University of Exeter, Exeter, UK

[2]Department of Geography, University of Exeter, Exeter, UK

[3]School of Geographical & Earth Sciences, University of Glasgow, Glasgow, UK

[4]Department of Geography and Planning, University of Liverpool, Liverpool, UK

[5]Universitat de Barcelona, Barcelona, Spain

[6]Mapua University, Manila, Philippines

Correspondence
Diego Panici, Centre for Resilience in Environment, Water and Waste (CREWW), University of Exeter, Exeter, UK.
Email: d.panici@exeter.ac.uk

Funding information
Department of Science and Technology, Philippines; Natural Environment Research Council, Grant/Award Numbers: EP/X527749/1, NE/S003312, NE/S003371, NE/W006871/1; Newton Fund, Grant/Award Numbers: X527749, W006871

Abstract

Alluvial river channels respond to changes in sediment supply by adjusting their geometry. Landslide sediment delivery and geomorphic response of river channels during floods are poorly understood and rarely examined in tropical settings. We investigate the impact of landslides on channel geomorphic changes during an extreme typhoon-induced flood event in the Philippines, specifically the complex geomorphic response of the Antamok River to Typhoon Mangkhut in September 2018, which triggered >500 landslides in the Ambalanga catchment. The catchment has a legacy of anthropogenic modifications, such as extensive small-scale (artisanal) mining and tailings storage facilities (TSFs) from large-scale mining activities.

We use a novel mix of mapping and computational modelling approaches to test the hypothesis that landslide sediment delivery is a major control on channel geomorphic change. Pre- and post-event imagery show that the overall active channel area increased by 35.9% and the mean active channel width increased by 9.1 m. Spatially, we find no clear relationship between landslide sediment input or unit stream power and channel width geomorphic change, with longitudinal changes in active channel width complicated by TSFs. Multi-phase modelling using r.avaflow revealed how landslide sediment delivery and TSFs interacted with the flow to generate the observed patterns of channel change. The model simulated channel incision in the upper parts of the catchment (up to 0.78 m) and deposition in the TSFs (up to 1.73 m).

Our findings demonstrate that well-established methods (e.g., stream power threshold) fail to fully explain channel width geomorphic changes, particularly for anthropogenically altered catchments. Integrating techniques, such as landslide mapping and multi-phase computational modelling improves understanding of sediment supply's role in channel width change during extreme events. Numerical simulations also demonstrate that conventional assumptions of increased erosion and deposition with rising flow discharge are inaccurate with large sediment input, highlighting instead the effectiveness of multi-phase models.

KEYWORDS
geomorphic change, hillslope-river linkage, landslide hazard, landslides, typhoon

1 | INTRODUCTION

Extreme rainfall events pose a serious hazard to human life and built environments (Catane et al., 2012) by causing rapid water level rise in river channels and the initiation of rainfall-triggered large mass-wasting cascading events (Iverson, 2000; Kirschbaum & Stanley, 2018; Paliaga et al., 2019; Stephenson et al., 2018), hereafter referred to as landslides, that may take place simultaneously (Catto & Dowdy, 2021; Iverson et al., 1997). Rainfall is known to be a major landslide trigger, even more than earthquakes in tectonically active regions (LaHusen et al., 2020). In particularly severe events, such as those caused by tropical cyclones, a single rainfall event can trigger up to thousands of landslides in a catchment (Abancó et al., 2021; Tseng et al., 2015). Moreover, the increase in intensity and frequency of extreme rainfall events caused by climate change is set to exacerbate this further (Gariano & Guzzetti, 2016). Landslide-channel interactions occur across different spatial scales, from the reach to the mountain-belt (Kirschbaum et al., 2019; Korup, 2005), mobilising large quantities of sediment that propagates through fluvial systems (Yanites et al., 2018), with a cascading effect on the geomorphology of channels at the valley floor (Zhao et al., 2017). The resulting changes can have a dramatic impact on sediment transport, channel capacity and thus flood risk (Nones, 2019; Slater, 2016; Slater et al., 2015). The hillslope-river linkage therefore controls a substantial component of sediment supply to fluvial systems (Korup et al., 2010; Wistuba et al., 2015). It is crucial to characterise the sediment input in landslide-prone areas where geomorphic processes can be significantly altered as a consequence of sediment transport (Church, 2006).

The impact of sediment delivery from landslides on downstream channel morphology may range from minimal geomorphic change (e.g., where fluvial erosion is the dominant process and landslides impinge minimally on the channel) to complete blockage and burial of the valley floor (Kirschbaum & Stanley, 2018; Korup, 2005). For example, intense sediment supply from landslides can dramatically affect the transport capacity of rivers (Benda & Dunne, 1997; Croissant et al., 2017; Ferguson et al., 2015), which results in change of slope (typically a localised lowering of slope) due to large volume of mobilised sediment and changes in bed morphology and sedimentology (Ferguson et al., 2015; Tseng et al., 2015). Often, sediment influx from landslides will see transient effects on the channel morphology, including aggradation followed by incision (Benda & Dunne, 1997; Rinaldi et al., 2005) that will release a sediment pulse (Ferguson et al., 2015) alongside changes in active channel width and disturbances to planform pattern (Benda & Dunne, 1997; East et al., 2017). For example, Croissant et al. (2017) observed that alluvial channel narrowing after large landslide input is a crucial process for rapidly allowing the passing of flood flow and sediment until the landslide deposit has been completely removed. Sudden sediment influxes from debris-flows and landslides typically widen channels over time by increasing the material on the channel bed or rapidly transporting sediment through the system (Nelson & Dubé, 2016; Rachelly et al., 2022). However, studying how landslides affect channel geomorphology and alter water flow is uncommon due to limited evidence post-flood and challenges in observing channel dynamics during these events. In extreme cases, a large supply of sediment from multiple shallow landslides concentrated within a short distance or from a large deep-seated landslide can overload the channel (DeLisle et al., 2021; Wistuba et al., 2015) and partially or completely block the flow (Catane et al., 2012; Dabiri et al., 2020; Paliaga et al., 2019), which may result in a sediment dam that can alter considerably the flow regime and channel morphology (Chen et al., 2017; Kumar et al., 2019) and pose a serious hazard to the downstream areas in case of dam burst (Dabiri et al., 2020).

To date, our understanding of how landslides affect channel flood conveyance and form dynamics is still in its infancy. Despite the likelihood of geomorphic hazards cascading downstream, only a few (e.g., Geertsema et al., 2022) systematic investigations of downstream channel change and the consequences for geomorphic-related hazards have been undertaken. While our ability to quantify and model geomorphic changes in river channels during normal flows is based on established approaches such as stream power thresholds or sediment transport capacity estimated from shear stress, these methods are considerably sediment-supply dependent (East et al., 2018) and may not be as accurate during high flows when a large quantity of sediment is delivered to the channel network (DeLisle et al., 2021), significantly affecting flow hydraulics and flow-sediment interactions. The upshot is that lateral sediment supply is rarely considered in existing fluvial morphodynamic models, because of the complex interactions between solid and liquid phases.

In this paper, we aim to identify and quantify the role of landslides in geomorphic changes of river channels during floods using a combination of novel models and techniques. Specifically, we investigate the impact of September 2018's Typhoon Mangkhut (locally known as Typhoon Ompong) on a tropical river in the Philippines by mapping landslide and channel changes, estimating changes in channel width and modelling landslide-channel interactions during the flood event using a multi-phase model – i.e., a model that describes the behaviours of liquid, solid and fine-solid phases and the interactions between them. We focused on the Antamok River in the Ambalanga catchment, on the island of Luzon, where a large number of landslides occurred in the 2018 event. As a result, we: i) mapped landslide and channel changes after landslides triggered by Typhoon Mangkhut; ii) estimated changes in the channel width and iii) modelled the interactions between landslide-generated sediment, river flow and channel morphology during the flood event using a multi-phase model.

2 | STUDY AREA

2.1 | The Philippines

The Philippines is one of the most typhoon-prone countries globally (Catane et al., 2012) with approximately 20 tropical cyclones entering the Philippine area of responsibility each year (Stephenson et al., 2018). Likewise, it is one of the most landslide-prone countries in Southeast Asia, and by extent, globally, recording a significant number of landslide-related fatalities each year (Froude & Petley, 2018; Kirschbaum et al., 2015). The effects of climate change are likely to increase the frequency of occurrence of landslides (Gariano & Guzzetti, 2016). Rivers in the Philippines are particularly dynamic, with fluctuating sediment supply from landslides (Abancó et al., 2021; Catane et al., 2012; Emberson et al., 2022), earthquakes (Atkinson, 1995), volcanoes (Gran et al., 2011) and anthropogenic activities such as dam construction for water supply, hydropower and mine tailings (Tabios III, 2020) contributing to globally high river

migration rates (Dingle et al., 2019). Emblematic of this dynamism, high rates of river planform adjustment have been observed in the vicinity of bridge infrastructure (Boothroyd et al., 2021).

We selected a segment of the Antamok River within the Ambalanga catchment as a test case to examine the channel geomorphic response to sediment delivered by rainfall-triggered landslides (Figure 1). Key reasons for selecting this study area include (i) a documented history of rainfall-triggered landslides (Abancó et al., 2021); (ii) a high density of landslides associated with a recent typhoon event (Typhoon Mangkhut, 2018) and (iii) considerable river channel changes associated with sediment delivery from the typhoon-event. Moreover, the catchment has a legacy of anthropogenic modifications, such as the presence of extensive small-scale (artisanal) mining (Ocampo & Schmitz, 2023) and mining tailings storage facilities (TSFs) associated with legacy and contemporary large-scale mining activities. These anthropogenic landscape impacts are common across mineral-rich catchments in the Philippines (Holden & Jacobson, 2012) and thus it is important to consider their impact on geomorphic response to extreme rainfall events.

2.2 | Catchment context

2.2.1 | Upper Agno catchment

The Upper Agno catchment (1,250 km^2) is in north-west Luzon, the largest island of the Philippines. Catchment headwaters are in the Southern Cordillera mountains with peaks up to 2,900 m.a.s.l and typically 30 to 60-degree slopes. The catchment is characterised by two pronounced seasons; dry from November to April and wet during the rest of the year (Tolentino et al., 2016). Most rain falls between June and September, coinciding with the South-West Monsoon. The mean annual precipitation for the Upper Agno catchment is 2,800 mm (1950–1993) and the mean annual runoff is 94.2 m^3/s (1946–1965) (Jayawardena et al., 1997).

Sediment load from the Upper Agno catchment has an important role in the operation and maintenance of three major dams: Ambuklao Dam, Binga Dam and San Roque Dam (Figure 1). Ambuklao Dam (built 1956) is a hydropower dam, one of the largest on the island. It ceased activity in 1990 due to a major earthquake in Luzon; the high rate of sediment inflow into the reservoir caused serious problems to the operation of the plant (Ehasz et al., 1992), but it was rehabilitated in 2011. Binga Dam (built 1960) provides energy for the peak demand of Manila and, therefore is nationally important. Finally, San Roque Dam (built 1998) is the largest dam in the country and one of the largest in the world. Given the crucial role of the dams in the Upper Agno catchment, it is particularly important to monitor the threat of sedimentation to them by cascading landslide hazards.

2.2.2 | Ambalanga catchment

The Ambalanga catchment (88.3 km^2) is a small headwater catchment of the Upper Agno catchment. The highest elevation is 1715 m.a.s.l.

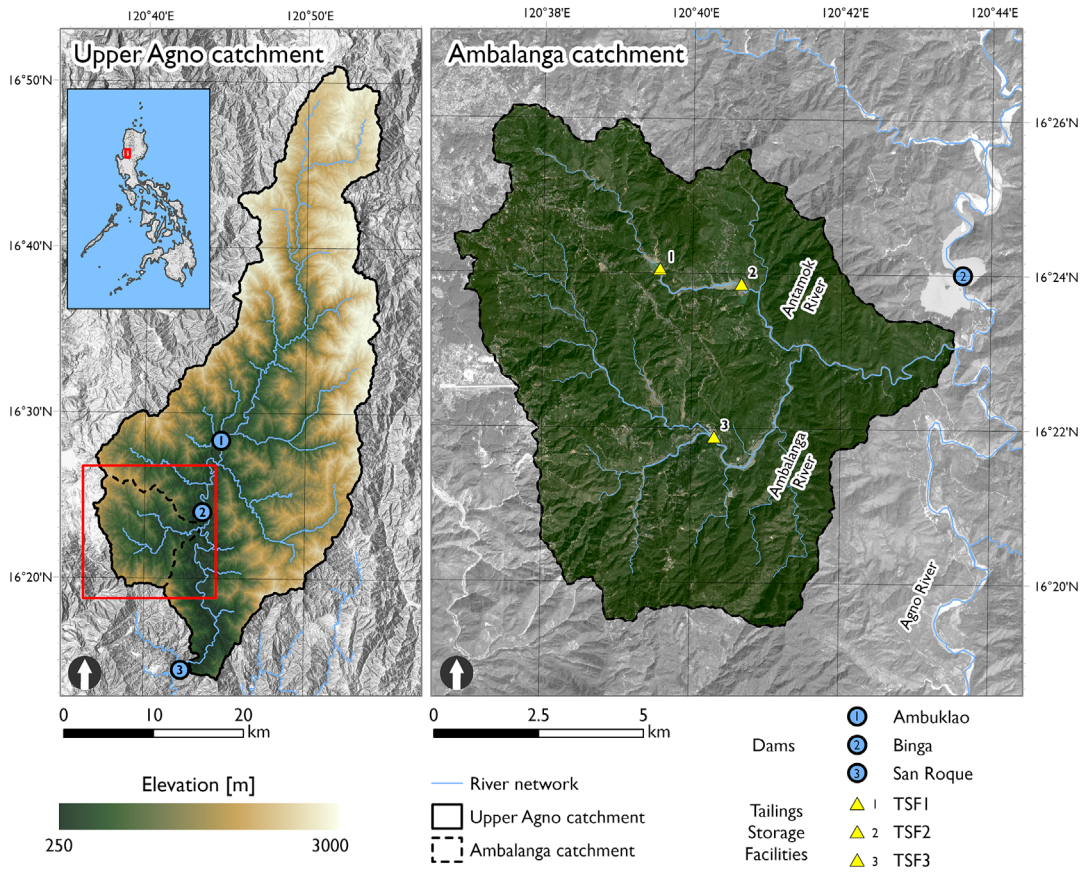

FIGURE 1 Location map of the upper Agno catchment and the Ambalanga catchment, including the main tributaries of the Ambalanga and Antamok Rivers. Major anthropogenic modifications to the river network include dams and several mine tailings storage facilities (TSFs). River centreline dataset is from Boothroyd et al. (2023).

and the mean slope value is 30 degrees, although the steepest slopes reach up to 76 degrees. The mixed sand-gravel bed Ambalanga and Antamok Rivers are the main tributaries in the catchment, entering the Agno River downstream of Binga Dam. Almost 90% of the soil is Bakakeng Clay (BSWM, 2012), a low plasticity and low permeability red clay, formed from the weathering of igneous rocks. The landscape has been considerably impacted by anthropogenic activities such as mining, which is common across mineral resource-rich catchments in the Philippines (Holden & Jacobson, 2012). Three tailings storage facilities (TSF) are located within the catchment, which were built by the Benguet Mining Corporation. We refer to these as TSF1 (also known as the Antamok TSF), TSF2 and TSF3. Human settlements within the catchment are barangays or villages of Itogon including Poblacion, Loacan, Ucab, Tuding and Virac. Whilst most literature refers to this catchment as the Ambalanga catchment (Macasieb et al., 2021a, 2021b), with the Antamok River as a tributary (Corpus et al., 2011), this catchment falls within the Itogon municipality so there are some local references to it as the Itogon catchment.

2.3 | Typhoon Mangkhut

Intense rainfall was recorded in the study area on 13 September 2018 and Typhoon Mangkhut made landfall on 15 September 2018 (National Disaster Risk Reduction and Management Council, 2018). The nearest rain gauge to the Ambalanga catchment is of the PAGASA Baguio Synoptic Station, located in Baguio City, measured a total amount of 791.4 mm, and a number of incidents associated with landslides and floods were registered (Weather Division PAGASA, 2018). Infrastructure, agriculture and buildings were affected by landslides, floods and river bank erosion. A landslide caused the death of 87 miners and their families in the area of Barangay Ucab (Ocampo & Schmitz, 2023; Palangdan, 2018).

2.4 | Preliminary evaluation of geomorphic effects of Typhoon Mangkhut in the Ambalanga catchment

The geomorphic effects of Typhoon Mangkhut on the Ambalanga catchment were substantial. Figure 2 shows the density of landslides that occurred (Abancó et al., 2021) and changes in active channel width from pre- and post-typhoon imagery (as detailed in section 3.1.2) to display the scale of change to the landscape for this event, and its relevance for our study. In the headwaters of the Antamok River a very high density of landslides was mapped (> 30 landslides/500 m radius). Channel widening was widespread and spatially variable in magnitude across the catchment. However, notable increases in segment-averaged active channel width were observed along the Antamok River, including a pronounced zone of sedimentation associated with a tailing site located at the downstream end of the segment (Figure 3a and b). Having identified the highest density of landslides and observed a considerable geomorphic response along the Antamok River, we selected this site for geomorphic change mapping and multi-phase modelling.

3 | METHODS

Channel geomorphic changes on the Antamok River during Typhoon Mangkhut were estimated by: (i) identifying from post-event satellite imagery the landslides within the river catchment, and then mapping

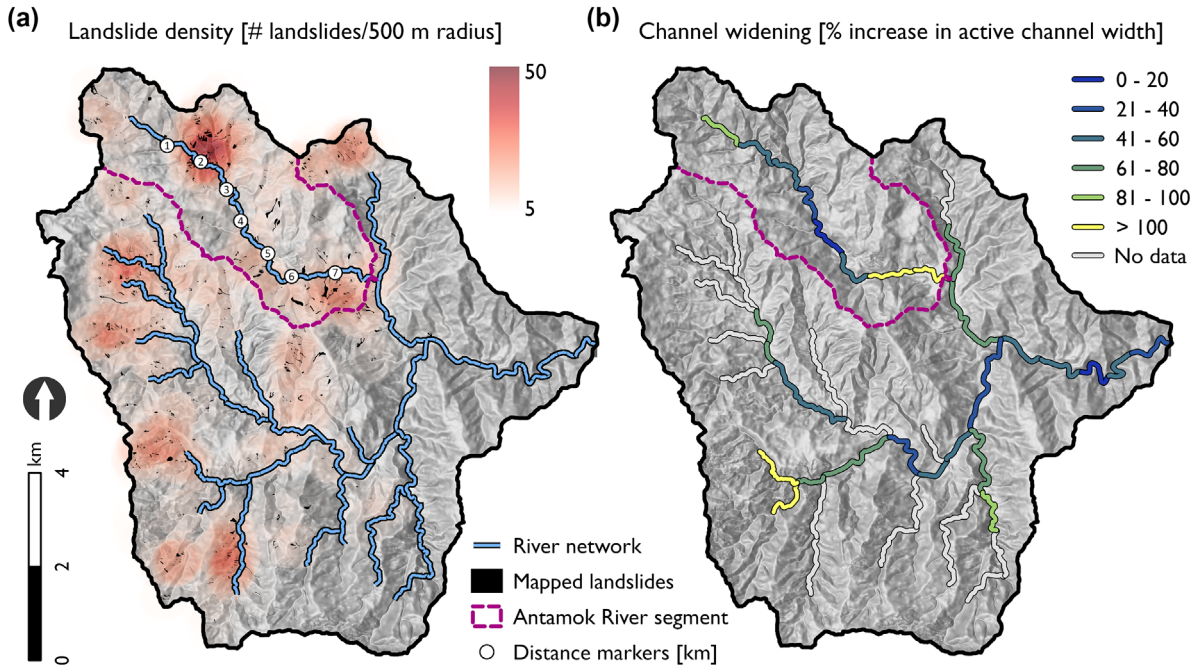

FIGURE 2 - Geomorphic effects of typhoon Mangkhut on the Ambalanga catchment, including the density of landslides and increases in active channel width. The density of landslides is from the landslide inventory published by Abancó et al. (2021). Highest values are located in the headwaters of the Antamok River. Increases in active channel width were averaged over segments approximately 1 km in length, using pre- and post-typhoon event imagery (explained in detail in section 3.1.2). Distance markers correspond to downstream distances in Figure 4.

FIGURE 3 - Sedimentation of TSF2 between 20/02/2018 (a) and 22/09/2018 (b). Image Centre is 16.39750°N 120.67473°E. Source: Google Earth.

the changes in active width of the channel; (ii) calculating the unit stream power for the flood flow and then comparing it with the observed channel width change and (iii) employing a multi-phase computational model to simulate the sediment delivery from landslides to the river network and the cascading effect on channel width change.

3.1 | Collecting landslide inventory and digitising active river channels and valley bottom extents

3.1.1 | Landslide inventory

We used an existing landslide inventory (Abancó et al., 2021). Landslides triggered by Typhoon Mangkhut were mapped manually, using 0.5 m resolution Pléiades and 10 m resolution Worldview satellite imagery, acquired between February 2018 and March 2019. The combination of imagery of different spatial resolutions allowed us to work with time windows as narrow as 13 days between pre- and post-typhoon images. A total number of 551 landslides and debris flows from the original 1,101 published in Abancó et al. (2021) are located in the Ambalanga catchment. Failure areas were defined by observing landslide features on the hillslopes of the catchment such as changes from densely vegetated areas to bare soil. Runout paths were distinguished, when possible, from the failure areas. They were identified by observation as elongated areas adjacent to the hillslope failure areas.

The majority of landslides occurred in Bakakeng Clay, whilst only two of the 551 landslides occurred in undifferentiated mountain soils, at the southern edge of the catchment. Landslides were less frequent on hillslopes of <20 degrees and >60 degrees, where the density was lower than 2 landslides/km^2. In contrast, there were up to 12 landslides/km^2 in hillslopes between 20 and 60 degrees. Most of the landslides occurred in forest and wooded land, although grassland, cultivated and built-up areas were also affected. As reported by Abancó et al. (2021), landslides mostly occurred in slopes facing East, South and South-East.

Delineation of failure areas was used to determine the sources of sediment. The volumes of landslides were estimated using a surface area-volume relationship (Guzzetti et al., 2009; Larsen et al., 2010), calculated as:

$$V = \alpha A^{\gamma} \quad \text{(Equation1)}$$

where V [m^3] is landslide volume, A [m^2] is landslide area, α [−] is a constant and γ [−] is an exponent. Based on an international database of soil landslides, we applied a constant of $\alpha = 0.664$ (±0.013) and an exponent of $\gamma = 1.145$ (±0.008) (Larsen et al., 2010). The estimation of the landslides area was done based on remote sensing (i.e., satellite imagery) observations. Most of the landslides were considered very shallow (2 to 3 m). Internal and basal friction angles of the superficial layers of the terrain, involved in the landslides, were estimated based on existing laboratory tests and descriptions of the soil types (Carating et al., 2014).

3.1.2 | Mapping active river channels

We digitised active river channels from Google Earth imagery acquired before and after Typhoon Mangkhut (Table 1). Google Earth imagery has previously been used to assess river channel form (e.g., Henshaw et al., 2020) and inter-annual patterns of planform change (e.g., Mandarino et al., 2020). Here we focus on mapping event-scale changes in the active channel. The active channel was manually digitised following the approach suggested by Winterbottom (2000) and similar to Collins & Sheikh (2004), based on the extent of the wetted river channels and alluvial deposits, including sparsely vegetated deposits. We defined the channel-margin delineation on the edge of continuous riparian vegetation, and minimised digitisation

TABLE 1 Details of Google earth imagery used to map pre- and post-typhoon event active river channels.

Image description	Image acquisition date	Image quality comments
Pre-typhoon event	19 February 2018	Generally good; some areas of orthoimage misalignment
	20 February 2018	Generally good; some areas of orthoimage misalignment
Post-typhoon event	19 September 2018	Generally good; some areas of cloud, cloud-shadow and orthoimage misalignment
	22 September 2018	Generally good; some areas of cloud, cloud-shadow and orthoimage misalignment
Background	17 October 2017 *	Generally good; some areas of orthoimage misalignment
	12 December 2019 *	Generally good; some areas of orthoimage misalignment

*Background imagery acquired from longer before/after the event to infill small gaps in the pre- and post-typhoon event imagery where issues with image quality were persistent (i.e., where cloud obscured the active river channel).

inconsistencies by having the same user complete the mapping procedure on both sets of imagery (Donovan et al., 2019). The mapped active river channel extents (vector data) were converted to a regular gridded product with 1 m spatial resolution (raster data) to quantitatively assess active channel change (see section 3.4).

3.1.3 | Mapping valley bottom extents

We used a nationwide digital elevation model (DEM) acquired in 2013 and generated through airborne IfSAR technology with 5 m spatial resolution and 1 m root-mean-square error vertical accuracy (Grafil & Castro, 2014) to map valley bottom extents. To define the extent of contemporary fluvial processes (Fryirs et al., 2016), we distinguished the margins of the valley bottom where either a break or change in slope was observed in the DEM and manually mapped the valley bottom extent. Due to the relatively small study area, we applied expert judgement rather than a semi-automated approach to valley bottom mapping (e.g., Clubb et al., 2022; Khan & Fryirs, 2020). The total area of the valley bottom extent for the Antamok River segment was 0.276 km^2. To ensure consistency with the data from section 3.1.2, we converted the valley bottom extents into a regularly gridded format with a spatial resolution of 1 m.

3.2 | Topographic and stream power analysis

3.2.1 | Topographic analysis

We used TopoToolbox V2 to delineate catchments from a nationwide DEM (Grafil & Castro, 2014) using standard flow-routing algorithms (Schwanghart & Scherler, 2014) with the D8 algorithm used to derive flow direction and a drainage area threshold of 1 km^2 to extract the stream network (Boothroyd et al., 2023). The position of the stream network was validated against the Google Earth imagery and showed good visual agreement. DEMs typically contain artefacts and errors that propagate into the calculations of local channel slope (Wobus et al., 2006). We used constrained regularised smoothing to minimise these effects along the stream network and smooth the channel elevation data (smoothing factor, $K = 2$; quantile, $\tau = 0.5$; Schwanghart & Scherler, 2017). This ensured downstream decreasing elevations and provided a hydrologically correct DEM. We imposed a minimum value (0.001 m/m) to avoid spuriously small values of channel slope. For context, the mean channel slope calculated from 128 medium- to large-sized catchments in the Philippines was 0.032 m/m (Boothroyd et al., 2023) and locally for the Antamok River segment the average channel slope is 0.07 m/m. Because stream network points were densely spaced (5 m spacing), topographically derived attributes vary over short distances (Ferencevic & Ashmore, 2012). To generalise these local fluctuations, we averaged derived attribute values over 100 m river segment lengths.

3.2.2 | Rainfall distribution

Hydrological data is limited in the study area, with continuous river flow records unavailable for most of the Upper Agno catchment. To estimate discharge, we therefore relied upon precipitation as an input for a simple approach to estimate the hydrological response to the event. We used satellite-derived precipitation data from the Integrated Multi-satellite Retrievals for Global Precipitation Measurement (GPM IMERG) mission to assess the spatial distribution of rainfall associated with Typhoon Mangkhut. The satellite-derived precipitation data has a spatial resolution of 0.1° and a temporal resolution of 30 minutes (Huffman et al., 2019). Accessed through Google Earth Engine, we calculated 24-hour rainfall totals, by summing 30-minute intervals, for the period 00:00 to 24:00 UTC on 15 September 2018. The 24-hour period was selected to coincide with the highest rainfall intensities of the typhoon event and followed a two-week period with considerable antecedent rainfall. Furthermore, the volumetric water content in the top 1 m of the soil on 15 September 00:00 appears to have reached its saturation point, according to SMAP-L4 satellite observations (Abancó et al., 2021). The rainfall totals were extracted as point data at the centres of GPM grid cells and then interpolated across the Upper Agno catchment using a regularised spline (weight = 0.1; n = 12). This provided regularly gridded 24-hour rainfall totals (100 m spatial resolution), used to indicate spatial heterogeneity in rainfall distribution.

3.2.3 | Discharge and stream power

To estimate discharge, we used satellite-derived precipitation data (Section 3.2.2) and outputs from the topographic analysis (Section 3.2.1). We assumed a steady uniform runoff and zero infiltration, based on the inference that the upper layer of the soil was saturated by this point of the rainfall event. We converted the gridded 24-hour rainfall totals [mm] into rainfall rates [m/s], to represent spatial differences in rainfall intensity across the catchment. The rainfall rates were used as weights in the calculation of flow accumulation, obtaining rainfall-weighted flow accumulation equivalent to an

instantaneous discharge [m^3/s]. Using TopoToolbox V2, the rainfall ratio of the flow accumulation was set to 1, meaning that all flow was transferred from each cell to its downstream neighbour. We acknowledge that the discharge values are indicative and likely overestimate the hydrological response to the event. The simplified approach assumes that rainfall instantaneously enters the channel with no transmission losses. It does not account for variation in infiltration rates, interception rates or travel times across the catchment.

Unit stream power was calculated as:

$$\omega = \gamma QS/w \quad \text{(Equation2)}$$

where ω is unit stream power [W/m^2], Q is discharge [m^3/s], S is locally smoothed channel slope [m/m], w is locally smoothed active channel width [m] and γ is the unit weight of water [kg/m^3]. We calculated the locally smoothed channel slope using a first-order Savitzky–Golay filter with a 50 m moving window (Bennett et al., 2016). We calculated the locally smoothed active channel width from the pre-Typhoon event imagery using a zero-phase filter (forward-reverse filter with a 250 m window size). We note the limitations of using the indicative discharge values as part of the unit stream power calculation; a more sophisticated discharge estimation approach would improve the physical representativeness of the stream power estimates. However, given the saturated conditions and dearth of discharge observations in the Upper Agno catchment, this approach was deemed appropriate for our analysis.

3.3 | Integrating results from mapping and topographic analysis

3.3.1 | Longitudinal patterns of landslides, active channel and valley bottom width

We split a DEM-derived stream network into 250 m sections and counted the number of landslide centroids located within 500 m of the stream network. This distance was chosen to indicate the proneness of a longitudinal channel section to landslide occurrence. We used the DEM-derived stream network as the reference centreline for estimating pre- and post-event active channel and valley bottom widths from the mapped outputs. We used the SWATHobj function of TopoToolbox V2 (Schwanghart & Scherler, 2014) to sum the number of mapped cells (1 m spatial resolution) perpendicular to the reference centreline, providing equally spaced estimates of active channel and valley bottom width along the stream network (5 m point spacing). The SWATHobj width was set to 500 m, which adequately captured the active channel and valley bottom extents, and a smoothing factor of 100 m was applied to reduce the reference centreline sinuosity over short distances. The overall swath length was 7.3 km. Spot checks of width estimates showed good agreement with manual measurements made in GIS (< ± 10% of measurement value). Active channel and valley bottom widths fluctuated locally; to reduce the noise associated with the estimates we applied a zero-phase filter (250 m window size). Although alternative approaches for deriving channel width may provide more accurate estimates (e.g., Golly & Turowski, 2017), the swath-based approach is advantageous in maintaining the same reference centreline for multitemporal analysis and enables multiple attributes to be co-located (e.g., landslide count, unit stream power, valley bottom width and active channel width).

3.3.2 | Quantifying changes in active channel width

Changes in active channel width were calculated as:

$$\Delta ACW = ACW_{post} - ACW_{pre} \quad \text{(Equation3)}$$

where ΔACW is the absolute change in active channel width [m], ACW_{pre} is the pre-typhoon active channel width [m] and ACW_{post} is the post-typhoon active channel width [m]. Positive ΔACW values indicate channel widening, whereas negative ΔACW values indicate channel contraction. We used ACW estimates with local fluctuations removed (zero-phase filtered) to identify longitudinally distinct behavioural zones (i.e., zones of widening).

3.4 | Sediment delivery from landslides to the channel (r.avaflow)

We used r.avaflow to model the contribution of landslides to channel geomorphic change. r.avaflow is an open-source software tool that is able to simulate complex mass flows across different landscapes. It can model different types of mass movements, such as landslides, avalanches, debris flows and lahars, and their interactions with each other and with the environment. The model operates by solving a system of partial differential equations that describe the conservation of mass and momentum of a multi-phase mixture of solid and fluid materials. The model works on a Non-Oscillatory Central difference-Total Variation Diminishing (NOC-TVD) numerical scheme (Wang et al., 2004) on a Voellmy-type model that has been amended with a multi-phase approach between solid and liquid phases, including energy or momentum transfer between phases (Mergili, Jaboyedoff, et al., 2020; Pudasaini & Mergili, 2019). This model was chosen due to its ability to model large, fast-flowing masses of sediment along river valleys, and its ability to output sediment deposition and erosion maps from the combined effects of landslides and flood flows. The model has been successfully used for a variety of applications, notably to simulate the geomorphic changes of the 2021 Chamoli disaster, the Indian Himalayas (Shugar et al., 2021). Fluvial applications of r.avaflow have studied the topographic change of river channels when large sediment volumes were introduced in the river network. For example, geomorphic change to mountainous river channels after debris flow mobility (Wang et al., 2023), entrainment of sediment in channels triggered by debris flow (Baggio et al., 2021) and channel changes from cascading rockslide-channelised debris flow (Mergili, Jaboyedoff, et al., 2020).

For elevations, in r.avaflow a DEM was employed as a baseline topography. For this purpose, we used the original 2013 DEM 5 m, and it was resampled using a bilinear algorithm to set a model grid size of 2 m. The model then required the definition of two further sets of input grids. The first set of input grids defined the release height of each phase, i.e., the volume of material that is initially released in a landslide per cell area. All sediment was released in the first time-step of the simulation and was set as the initial condition, together with the flow hydrograph. The input values for set one of the input grids

were estimated from the erosional areas that have been manually mapped (as discussed in section 3.1.1). The distribution of depths between (i) coarse, non-cohesive sediment, displaying plastic behaviours and friction dominated (referred to hereafter as the "solid" phase), and (ii) fine sediment showing viscoplastic behaviours and dominated by friction and viscosity, referred to hereafter as the "fine-solid" phase, were based on the geological and geotechnical properties of the soil in the area, which were estimated to be 45% and 55% for solid and fine-solid phases, respectively, based on information on soil types (Bureau of Soils and Water Management, 2012). The second set defines the maximum entrainable depths, that is, the height and extent of terrain that could be eroded and entrained by a flow. Here, these were released volumes of solid and fine-solid and coincided with the mapped areas of landslides and run-outs. The error in the landslide depth estimation was not considered for the modelling exercise. However, a sensitivity analysis of the model to change in erodible depths was undertaken (section 5). This showed predictions to be relatively insensitive to this.

Input hydrographs were placed within the channel network and based on the estimation of the flow discharge in section 3.2.3; each input hydrograph was placed at the headwaters of the channel network and values of discharge were assumed constant throughout the simulations, which had a duration of 600 s.

The computational model employs a wide range of parameters for simulations. We investigated the variation of the parametric space by varying the key-parameters of internal friction angle, basal friction angle and drag force exponent, where initial values were chosen on the base of typical values for soils observed in the River Antamok catchment. The choice of parameter values was then fine-tuned to best fit the observed changes in channel morphology, that is the extent of active channel area. Since the model could not be validated against observed data of sediment fluxes (as this was not available), a sensitivity analysis testing different combinations of parametric values was undertaken (section 5.2). A series of flux monitoring points along the channel network were defined to record model predictions during the 600 s duration simulation time. The model outputs for each phase included: discharge [m^3/s], velocity [m/s] and depth of flow (individually for solid, fine-solid and fluid phases) [m].

4 | RESULTS

4.1 | Relationship between landslides, stream power, valley bottom width and active channel change

Figure 4 shows the longitudinal patterns of landslide inputs, topographic attributes and active channel change over the 7.3 km length of the Antamok River segment, which are also summarised in Table 2. Landslides have occurred along the full length of the segment, but landslide counts and volumes within 500 m of the channel centreline are spatially variable. The largest centroid counts, ranging between 28 and 41, were recorded in a cluster between downstream distances of 1.5 to 3 km (Figure 2). Volumetrically, the inputs associated with this cluster were considerable, ranging from 49,800 to 129,000 m^3. A second cluster of landslides was recorded at the downstream end of the segment (6.75 to 7.5 km), with a lower number of centroid counts (ranging from 9 to 17) but a greater landslide volume (ranging from 101,000 to 141,000 m^3). The counts and volumes of landslide inputs in the remaining zones were comparatively lower. Combined with the landslide density map (Figure 2A), we observe longitudinal variability in the patterns of landslide inputs.

Discharge increases approximately linearly in the downstream direction from 1.88 to 26.43 m^3/s due to the simplified approach used to estimate discharge. Channel slope is variable but generally steep (mean slope = 0.07 m/m; median slope = 0.07 m/m; standard deviation of slope = 0.06 m/m). A zone with a constantly low channel slope at a downstream distance of 5.40 to 6.70 km is influenced by anthropogenically modified drainage around the mine TSF and is caused by imposing a minimum channel slope (section 3.2.1) – this is the area corresponding to a very large channel widening (that is, the mine TSF impoundment). Unit stream power is variable along the segment. Discrete peaks in unit stream power are caused by local increases in channel slope and/or reductions in channel width (e.g., upstream of the TSF dam at a downstream distance of 4.95 km; maximum unit stream power = 5,570 W/m^2). Unit stream power is low (< 200 W/m^2) where the channel slope decreases and/or the channel widens (e.g., downstream distances of 3 to 4 km and parts of the segment influenced by the TSF dam).

Valley bottom widths (VBW) and active channel widths (ACW), Figure 4D and E, respectively, show longitudinal variability. In general, the valley bottom is narrow (< 50 m width) although there are several locations where the valley bottom widens (up to a maximum width of 231 m). Longitudinal changes in valley bottom width are useful to identify constrictions where the valley narrows over short distances (e.g., at a downstream distance of 4.05 km) and expansions where the valley widens over short distances (e.g., at the upstream end of the TSF, at a downstream distance of 5.15 km). In the pre-event imagery, the mean active channel width was 24.9 m; this increased to 34.0 m in the post-event imagery. The standard deviation of active channel width remained approximately consistent ($\sigma ACW_{pre} = 51.2$ m; $\sigma ACW_{post} = 54.0$ m. The correlation coefficients between active channel widths and valley bottom widths are positive and strong ($ACW_{pre} = 0.90$; $ACW_{post} = 0.89$). It follows that variation in valley bottom width exerts an influence on active channel width due to the confining effect of the valley bottom margin. We note that maximum values for pre- and post-event active channel width exceed the maximum valley bottom width; this can be explained by the different data sources, timings and resolutions of data acquisitions (valley bottom width from a DEM acquired in 2013; active channel width from optical imagery acquired between 2017 and 2019).

Comparing the pre- and post-event imagery, the mapped active channel area increased from 0.174 to 0.236 km^2 (35.9% increase). The longitudinal patterns of active channel change show that lateral adjustments are not spatially uniform; lateral adjustments are localised, and the magnitude of adjustments vary longitudinally (e.g., Figure 3 where widening varies substantially). In terms of active channel width changes in Figure 4f and g, the highest magnitude changes occurred as channel widening at downstream distances of 2.8 to 3.3 km (widening of up to 36.9 m) and downstream distances of 5.0 to 6.5 km (widening of up to 37.1 m; associated with reworking in the TSF). Because active channel width varies by more than two orders of magnitude along the Antamok River segment, width changes were converted into percentage changes. Expressed as percentage change, the highest magnitude change occurred in the zone

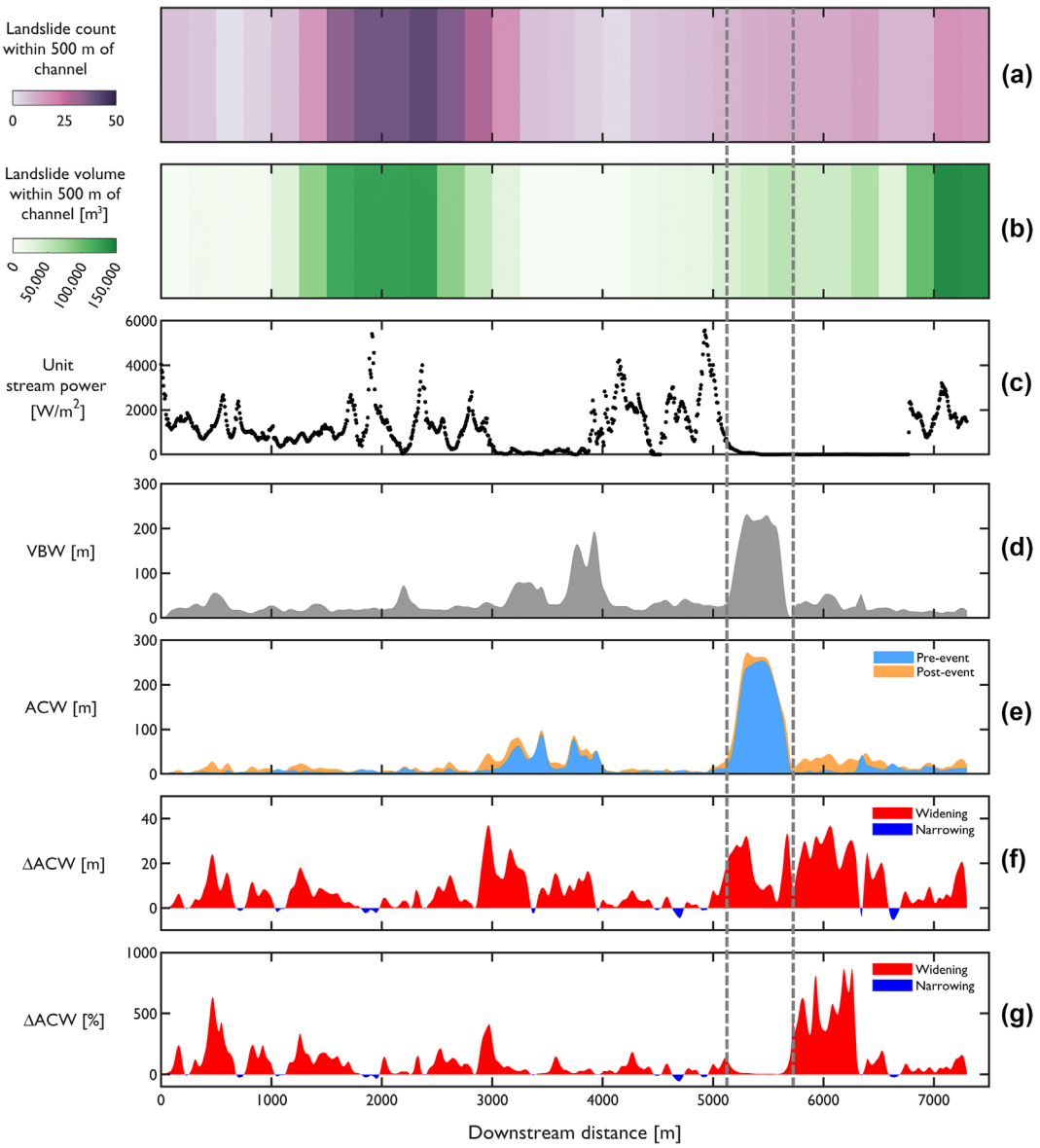

FIGURE 4 - Longitudinal patterns of landslide count, unit stream power, valley bottom width (VBW) and active channel width (ACW) along the Antamok River. Grey dashed line indicates the position of TSF1.

TABLE 2 - Derived topographic and active channel attributes along the Antamok River segment.

	Mean	Median	Standard deviation	Minimum	Maximum	Range
Elevation [m]	994	984	136	803	1,305	503
Discharge [m^3/s]	14.2	14.9	7.4	1.9	26.4	24.6
Channel slope [m/m]	0.0688	0.0682	0.0578	0.0001	0.3066	0.3065
Unit stream power [W/m^2]	992	817	1,019	0.1	5,570	5,570
VBW [m]	43.9	26.2	49.3	3.0	231.4	228.4
ACW_{pre} [m]	25.0	7.3	51.2	1.0	253.8	252.8
ACW_{post} [m]	34.1	15.4	54.0	1.0	272.0	271.0
ΔACW [m]	9.1	6.4	9.4	−5.3	37.1	42.4

immediately downstream of TSF1, shown in Figure 4g (up to 866% of widening, locally). We note that although widening was the dominant lateral adjustment process, small zones of low magnitude narrowing were also observed (e.g., 4 m of narrowing at a downstream distance of 4.7 km). The correlation coefficient between valley bottom widths and active channel changes was positive but negligible (correlation coefficient = 0.23). Furthermore, the discrete peaks (Figure 4c) in total unit stream power are not directly associated with zones of pronounced geomorphic change. Rather, for some reaches there appears to be a spatial lag between peaks in unit stream power and zones of

lateral adjustment (e.g., at the entrance to TSF1). Moreover, two reaches were characterised by an inverse association, whereby zones of low unit stream power (<200 W/m^2) are associated with considerable active channel widening (e.g., at a downstream distance of 3 to 4 km). Overall, the channel geomorphic response to Typhoon Mangkhut is spatially variable and not well explained by landslide inputs, longitudinal changes in valley bottom width or unit stream power; all of which are complicated by mining infrastructure (e.g., the presence of TSF dams) and the natural heterogeneity of the hillslope-river system.

4.2 | Computational modelling of geomorphic change during Typhoon Mangkhut

The model results show that sediment delivery to the channel is predominantly impulsive and of short duration. Figure 5 displays the value in time of the solid phase height. Each tile shows topographic change for a different time interval during the first 180s of simulation; this time period encompasses the development of most landslide phenomena and channel transport, following which little movement is observed during the rest of the simulation time. This also indicates that predicted sediment delivery to the channels is predominantly impulsive and short-lived. Figure 6 shows the final topography of the study area after the simulation has been completed, highlighting the topographic change in the vicinity of the TSF1 and TSF2 dams. Two areas of interest where different phenomena can be observed are detailed below (Figure 6a and b).

In general, model predictions indicate that complex spatio-temporal patterns of erosion and deposition occurred during Typhoon Mangkhut. Deposition within the channel was only observed in the presence of sharp bends or where a large volume of sediment was delivered by landslides. A notable case, identified in Figure 6a, showed that a potential instream sediment dam might have formed,

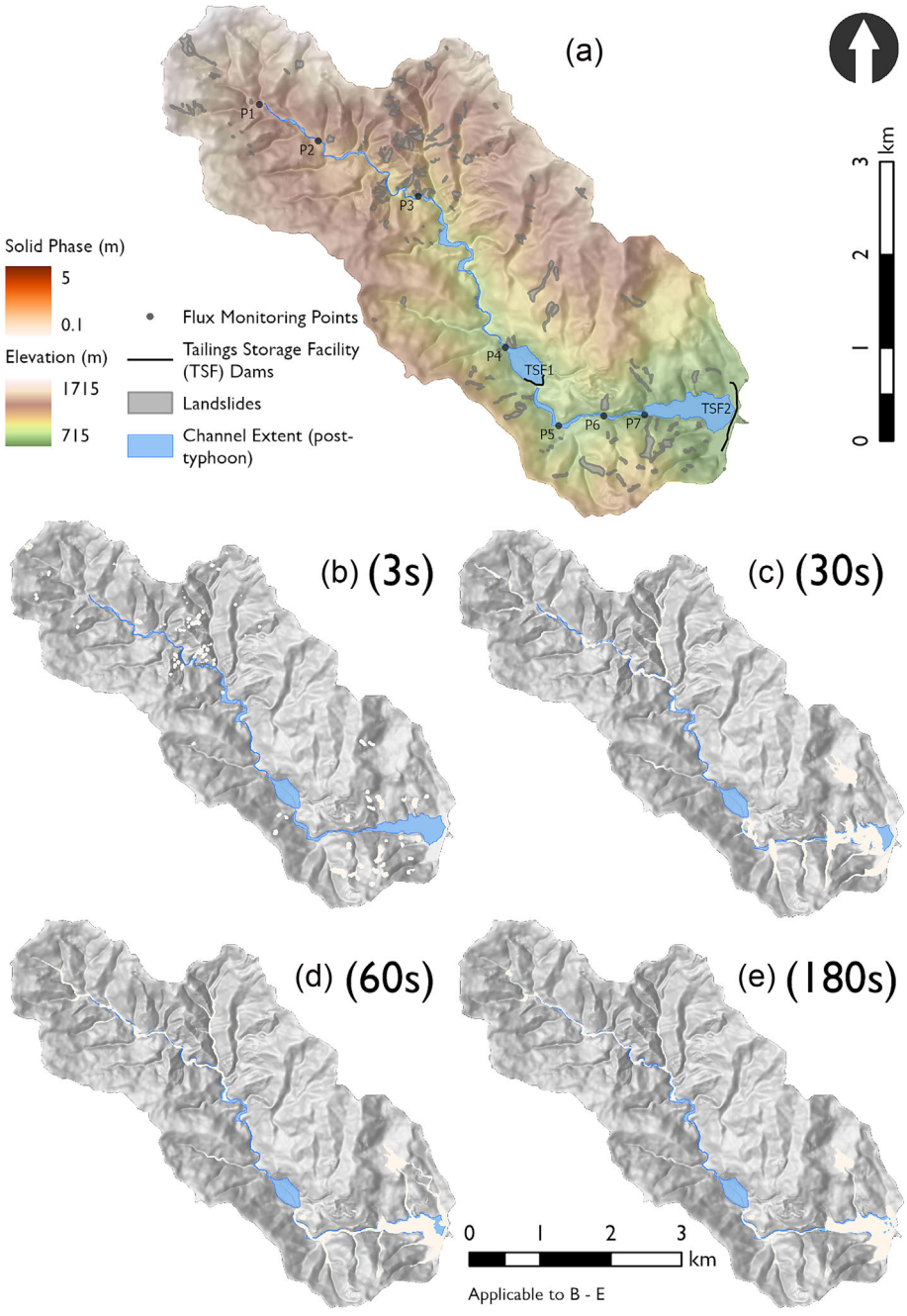

FIGURE 5 – (a) Antamok River study area modelled in r.avaflow, with flux monitoring points (P1–7) and tailings storage facility (TSF) dams. (b) To (e) temporal evolution of simulated solid flow; the solid flow height is the combined height of solid and fine-solid phase heights.

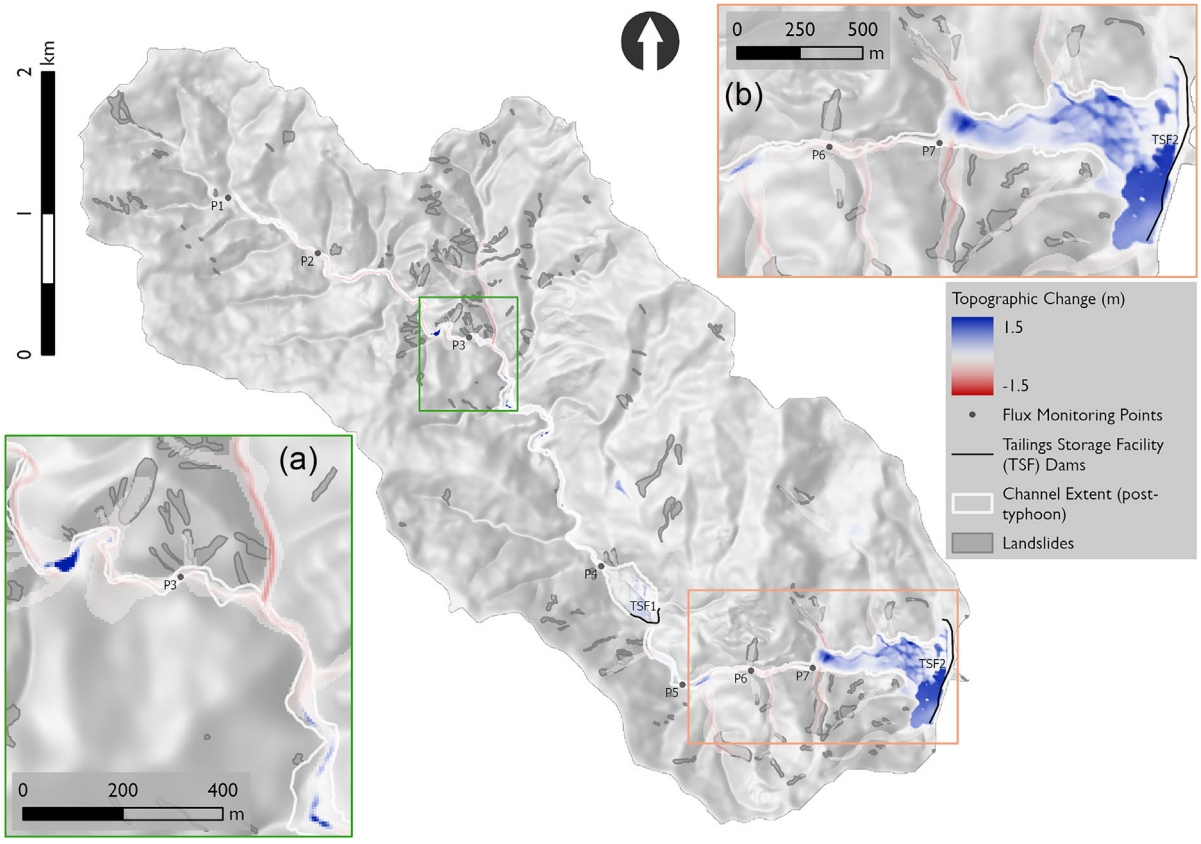

FIGURE 6 – Topographic change of the catchment of the Antamok River modelled by r.avaflow overlaid on the pre-event DEM and compared to the observed pattern of channel widening and landsliding. Predicted erosion and deposition are shared red and blue respectively. Two areas of interest (a and b) are shown in greater detail. Points of interest (labelled P1-P7) are indicated and used to analyse the temporal evolution of the simulated flows at flux monitoring points.

shortly downstream (<50 m) of an influx of landslide sediment. Another important insight is that deposition largely occurred at or in proximity to the TSF dams. This is especially evident for TSF2 (Figure 6b), where the depth of deposited sediment reached a peak of 1.725 m. On the other hand, erosion occurred widely across the study area, in most cases as incisions along landslide runouts and within the channel, with depths of erosion ranging from −0.115 m to −0.775 m. In the area downstream of TSF1, corresponding with Figure 6b, the fatal landslide and neighbouring landslides, erosional activity is more evident on the runouts than in the upstream areas. Overall, it can be observed that the part of the study area enclosed between TSF1 and TSF2 is the most active for both erosion and deposition.

A measure of the sediment delivered from landslides to the channel network can be observed from several flux monitoring points (Figure 7). Peak discharges tend to occur either as single (e.g., P1 and P3) or multiple maxima (e.g., P2). For the former, sediment influx is normally from a single landslide and when the bulk of the sediment is delivered to the channel this shows as a large spike in solid discharge. For the latter, the multiple peaks are due to the contribution of several different landslides that get delivered at the flux monitoring point at different time frames; although all landslides in the model are released at the same time, the time to reach different reaches in the channel network varies between different landslides. This would also indicate that sediment discharges originating from multiple concurrent landslides are unlikely. For example, at P2, the first two spikes (between 0 and 120 s) originate from nearby landslides; however, the third and largest spike (at approximately 135 s) is very similar in magnitude (430.4 m^3/s, compared to 384.6 m^3/s) to the large spike recorded at P1, which is shortly upstream of P2, just 54 s earlier; this may indicate that the landslide causing this sediment discharge spike is the same for both P1 and P2 (Figure 7a).

A further observation can be made at P3; in this case, a large spike (892.1 m^3/s) is observed early in the simulation (24 s), which can only be caused by the landslides immediately next to the flux monitoring point. A relatively negligible solid discharge is observed later, whilst a large deposition occurs immediately upstream of P3. This might indicate that sediment in the peaks of P1 and P2 was deposited along the river channel before reaching P3 and only a small part was delivered in the downstream areas. Eventually, the sediment delivery to TSF1 is essentially due to nearby landslides rather than an overall contribution from the whole catchment. This was not observed in the lower area of the catchment. Here, the majority of the solid discharge is delivered to the impoundment of dam TSF2 without being deposited first along the channel. This different behaviour compared to the upper catchment is potentially due to the much shorter distance between the headwater and the TSF dam, significantly reducing the potential for deposition.

Average velocities of sediment were impulsive and short-lived for all points of interest in the Antamok River study area. Figure 7 shows the average velocity of the solid phases at flux points in the Antamok River study area. Peak solid phase velocities correspond to peak solid discharges, whilst very low values are observed in non-peak

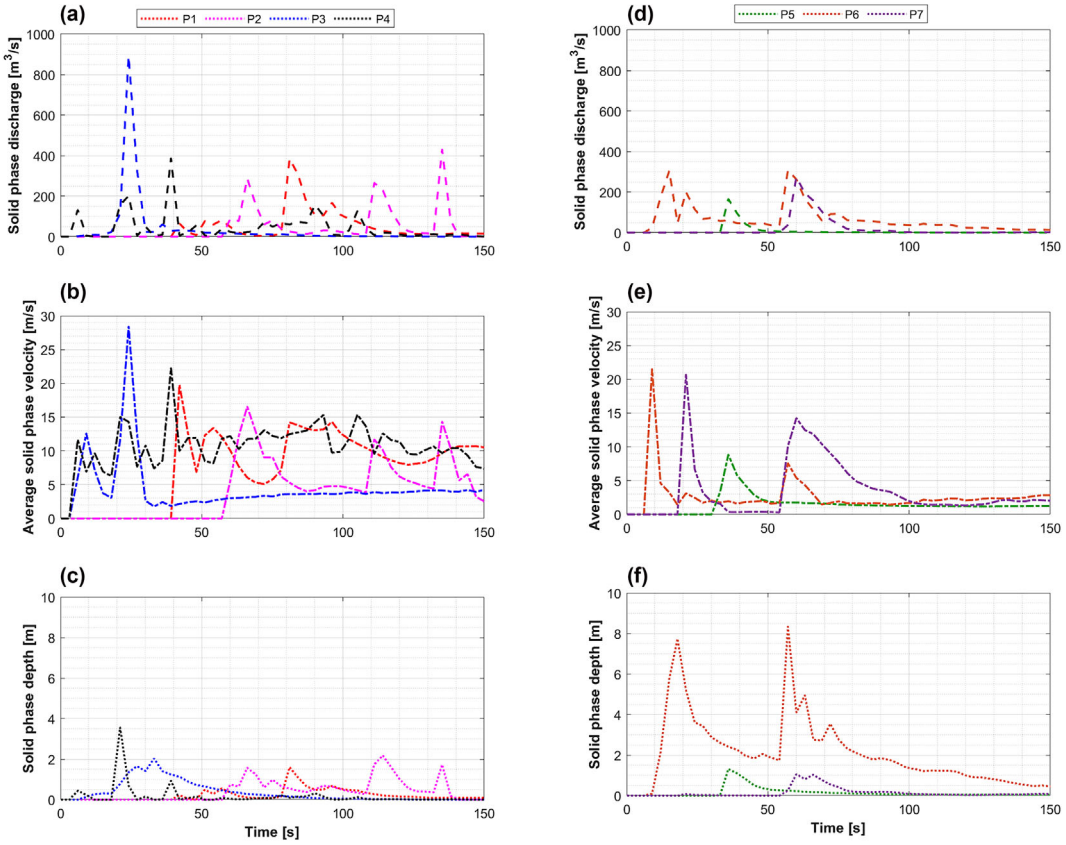

FIGURE 7 – Solid flow (solid and fine-solid) quantities from r.avaflow simulations at flux monitoring points in the Antamok River study area. Top to bottom: solid discharge (a and d), average solid velocity (b and e), solid depth (c and f). Left, flux monitoring points upstream of TSF1 (a, b, and c). Right, points of interest in between the two tailings storage facility dams (d, e, and f).

conditions, with the notable exception of velocity for P4 on the upper catchment. In this case, the average velocity for both solid and fine-solid phases is consistently above 10 m/s, despite discharges being relatively low. This can be explained by the very low solid flow depth (also shown in Figure 7) that is simulated in this particular section. Point P4 is located upstream of TSF1, which results in a channel width expansion. Finally, flow depths towards the downstream end of the catchment are lower than those at the upstream end. The only exception is P6, where the solid flow depth is higher than any other flux monitoring point as it coincides with valley confinement and channel narrowing. Sediment delivered from upstream and nearby landslides thus tends to back up at this location, although is eventually mobilised to the downstream TSF. At this location, solid phase velocity peaks ahead of the solid discharge, indicating that the kinetic component of the flow energy is then slowed down, despite an increase of the solid flow.

5 | DISCUSSION

5.1 | General observations

The first key finding is the limited association between discrete peaks in unit stream power and active channel change. Whilst stream power is a widely used indicator of the capacity of rivers to erode and transport sediment (Bizzi & Lerner, 2015; Jain et al., 2006) and has been used to explain the geomorphic response to floods (e.g., Magilligan et al., 2015), in this study it does not explain the observed patterns of channel change (Figure 4). Our findings are in agreement with previous studies that showed a limited association between unit stream power and observations of alluvial channel change (Parker & Davey, 2023). Unit stream power gradients have previously been used alongside channel confinement to predict the reach- and segment-scale response of channels to floods (Sholtes et al., 2018). Here we identified at least two reaches where zones of lowest unit stream power were associated with considerable channel widening. Antecedent conditions and the presence of TSFs may complicate stream power associations (East et al., 2018). Manual mapping and topographic analysis would suggest that a large amount of sediment delivered downstream of landslide sites substantially affected the geomorphic response of the channel, although with limited correlation in space or with sediment volume. It could be also possible to infer that the simultaneous occurrence of abrupt input of landslide sediment and channel narrowing in space would increase sediment transport capacity, potentially suppressing the depositional response to landslide sediment input. Nevertheless, there is no obvious correlation that could consistently support this option. On the other hand, multiphase modelling has helped to reveal how landslide sediment supply and TSF dams have interacted with the flow to generate the observed pattern of channel change.

Bennett et al. (2017) suggested a relationship between landslides and channel widening, whereby landslides may amplify the pattern of channel erosion and widening through damming and bulking the flow with sediment. However, this finding was made in a relatively pristine

mountain catchment in Colorado. In this study, the catchment is impacted by mining and TSF dams that interrupt the flow and connectivity between hillslopes and the channel (Barman et al., 2018; Kondolf, 1997). Similar to Bennett et al. (2017), this study finds that the standard hydro-geomorphic method of stream power failed to explain the observed pattern of geomorphic change. However, unlike Bennett et al. (2017) the relationship between landslides and channel change in this study is complicated by compounding effects of complex antecedent conditions and human land use - e.g., mining (Cox et al., 2021; Dethier et al., 2023). The highest concentration of landslides occurred between 1,500 m and 3,000 m downstream of the Antamok River headwaters, whilst the largest channel widening occurred in the channel reach downstream, between 3,000 m and 4,000 m. This may suggest a spatially-lagged response of channel widening to landslide sediment input, a speculation supported by the observation that channel width change further downstream is limited, corresponding with the area with the smallest number of landslides. The area downstream of TSF1 was also highly affected by channel widening, corresponding with several large landslides including the fatal landslide in Barangay Ucab.

The multi-phase model, r.avaflow, was shown by Bennett et al. (under review) and Bennett et al. (2024) to effectively simulate the role of landslides in channel geomorphic change in an extreme flood event. However, prior to our study, it has not been used to simulate geomorphic change in a catchment both heavily impacted by landslides and mining. The limitations encountered by stream power approaches were not observed with r.avaflow simulations when compared to the observed topography. In general, the topographic change of the channel extents simulated by r.avaflow qualitatively followed the manual mapping, as shown in Figure 6, including in those areas where stream power showed inconsistent results. For example, downstream of a large cluster of landslides in Figure 6a, the computational simulations nearly matched the observed channel extent. Although most of the channel change was accurately simulated, some localised areas were not correctly captured by the computational simulations. For example, Figure 6b shows some substantial erosion on the left bank of the river, which could not be modelled by r.avaflow. It should also be considered that r.avaflow simulations are carried out with a simultaneous release of sediment from all landslides, and therefore different erosive-depositional patterns might be observed when sediment is released at different time instants, although the observed flows and heights in Figure 7 would suggest that overlapping between landslides is generally unlikely. It should also be noted that drainage in the vicinity of the TSFs is complex; following this remote sensing and numerical modelling study we had the opportunity on another project to visit the catchment and that demonstrated that there were some underground flow diversions around TSFs. In the future, such diversions could be considered in numerical modelling.

5.2 | Sensitivity analysis of numerical modelling

We performed a sensitivity analysis on the parameters used within r.avaflow to assess model robustness (Table 3). Figure 8 shows the two areas of interest for seven different scenarios; Test 1 being the baseline model and the remaining six having a single parameter changed at a time. Change in drag coefficient (Test 2) from linear to quadratic had minimal effects on the simulations, suggesting very limited sensitivity of the model. On the other hand, in Test 3 the model is selected to be a simple solid phase (i.e., all sediment release by landslides and eroded within the catchment has no fine-solid component that displays viscous features, similar to debris flow-like landslides), and in this case the difference is substantial. Eroded areas are almost exclusively the landslide run-outs (except for some channel areas in the area of interest 2), whilst generalised deposition occurred along the main channel in the upper catchment, in contrast with both manual mapping and other simulations. Therefore, this particular combination of parameters did not capture the observed phenomena and suggested that differentiation between sediment with viscous and non-viscous effects is crucial for the right modelling exercise.

TABLE 3 – Summary of sensitivity test analysis for tests 1–5 with indication of the type of parameter or quantity tested.

Test	Parameters or quantities tested
Test 1 (baseline)	N/A
Test 2	Drag coefficient = 1
Test 3	Only frictional effects
Test 4	Internal friction = 25° for solid and 20° and for fine-solid phases
Test 5	Entrainable heights +50%
Test 6	Input discharge +20%
Test 7	Input discharge −20%

Notably, this finding is in contrast to simulations run by Bennett et al. (under review) and Bennett et al. (2024) which reproduce the observed geomorphic change without a fine component of the solid flow based on the different geology of their study catchment. This highlights the importance of properly parameterising the model based on the geology of the study area. Test 4 simulated values of internal friction for each phase smaller than the baseline model (25° and 20° for solid and fine-solid phases respectively, against 35° and 25°). There were no noticeable differences observed, suggesting that for this type of problem, the internal friction has low sensitivity. Test 5 simulated increased entrainment, i.e., the height of entrainable material for each computational cell was increased by 50%. Some differences may be noted, especially in the distribution of solid flow depth in the area of interest 2, but even for this case the simulations proved to be only mildly sensitive.

Finally, Tests 6 and 7 simulated a 20% increase and decrease, respectively, of the input discharge. These tests were undertaken to evaluate the performance of the model with uncertain values of discharge (see section 3.2.3 for the discharge estimation method). Both tests showed limited differences when compared to Test 1 (e.g., small changes in deposition patterns within Area A and Area B). Thus, it can be assumed that uncertainty in input discharge has a limited influence on the r.avaflow simulations. Interestingly, both Tests 6 and 7 showed a slight localised reduction in eroded areas within the upstream channel reach of Area A. It is unclear what caused this difference, although it might be a result of the fluctuations in model outputs with variations of discharge, or feedback loops (e.g., sediment supply and capacity) within this localised area of the system that are not immediately evident. The results in Figure 8 also show that assumptions on

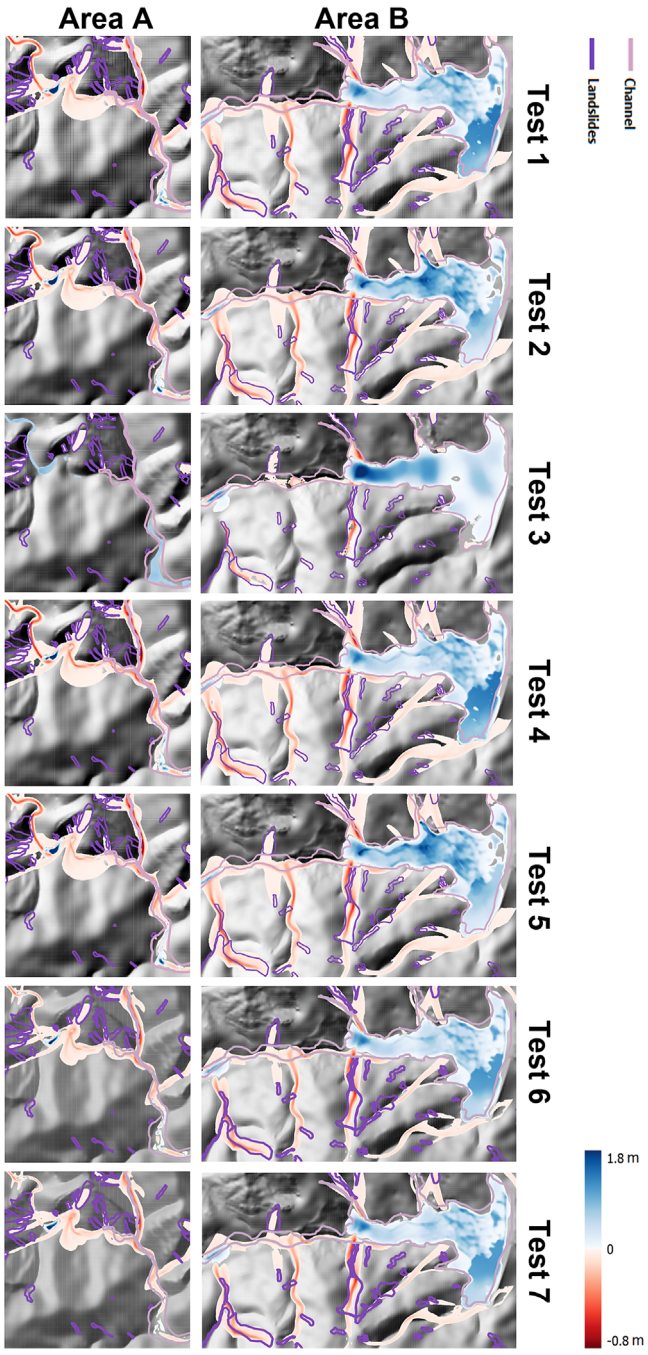

FIGURE 8 – Simulations at the two areas of interest testing different parameters (areas shown in Figure 6). Tests refer to the baseline (test 1) and one-at-a-time sensitivity analysis on linear drag (test 2), single phase (coarse) sediment (test 3), angular friction reduction (test 4), entrainment increase (test 5), discharge increase (test 6), and discharge decrease (test 7). Colour scales indicate topographic change, whilst pink and purple outlines represent post-event channels and landslides, respectively.

precipitation-derived discharge methods (as per section 3.2.3) only modestly affect channel morphodynamics modelled by r.avaflow. Sediment transport capacity that has been predicted using shear stress relationships has been observed to vary by several orders of magnitude when the uncertainty associated with modelled rainfall-derived discharges is considered (Keck et al., 2022). The lower variation shown by our uncertainty analysis is principally caused by r.avaflow predicting a multi-phase mixture of solid and fluid materials; predictions are thus less sensitive to changes in flow input because of the importance of the solid phase, and energy and momentum exchange between phases.

The simulations using r.avaflow showed that overall, there is consistency between the observed and simulated post-flood channel, although some limitations were observed consistently across the simulations. For example, it is unclear why some areas of substantial erosion were not reproduced (e.g., the left bank of the channel upstream of the TSF dam in the area of interest 2). Furthermore, solid discharges seem to occur impulsively, i.e., sediment delivery to the channel network and subsequent transport occurs in a short timeframe, whilst sediment velocity seems relatively high (e.g., in several points velocity of the solid phase is consistently higher than 10 m/s). Nevertheless, velocities of this magnitude are not uncommon, since similar observations have been made in Switzerland (Schlunegger et al., 2009), Japan (Suwa et al., 2009) and Italy (Arattano & Marchi, 2005), for channels displaying similar slopes and geometry to the River Antamok catchment. They are also comparable with other r.avaflow simulations on landslide-channel connectivity on mountainous or steep catchments (Mergili, Jaboyedoff, et al., 2020; Mergili, Pudasaini, et al., 2020), consistent with the channel gradient in the study area that has been simulated here, that is typically steep (i.e., approximately 4° or 0.07 m/m). Thus, it is not unrealistic to expect flow and sediment velocities that are substantially higher than lowland rivers.

Consideration should be given to the change in connectivity between hillslopes and channels due to mining activities since the catchment hosts numerous small-scale mines and several TSFs from large-scale mining. Mining is known to have impacts on vegetation cover and can undermine hillslopes, resulting in increased erodibility and instability of hillslopes (Tarolli & Sofia, 2016). Indeed, concerns about slope stability due to networks of mining tunnels have been raised in this catchment (Ocampo & Schmitz, 2023). Thus, mining activities may increase the size and frequency of landslides, which may increase sediment flux, depending on location and distance from the sediment source. However, TSF dams in this catchment also have a role in storing sediment (James, 2013) and have the potential to substantially alter sediment transport within a particular river network (Wohl, 2015), as is visible from our investigation. Results from r.avaflow, as discussed in section 4.2, showed that the catchment upstream of TD1 had most of the sediment input from landslides deposited before reaching the TSF. The solid discharge (as per Figure 7, point P4) is small compared to other upstream points of interest, therefore the impact of this TSF dam is limited, with only small areas of deposition. On the other hand, TSF2 showed a substantial capacity for trapping sediment, displaying very high deposition and solid discharges, together with a significantly wider channel than other areas. This different behaviour can be explained by: (i) the larger sizes of landslides in the downstream parts of the study area and (ii) the shorter travelling distance between landslide input into a channel section to the TSF, compared to the upstream parts of the study area. Thus, it can be inferred that connectivity between landslides and TSF dams strongly depends on the distance travelled and the volume of sediment released within the channel.

Overall, in the specific area analysed in this paper, the increase in landslides may have a limited impact on TSF1 (in consideration of the reduced delivery of sediments from upstream areas). However, it

might be expected that the increase in sediment delivery to TSF2 would be substantial. This will have a significant impact on the TSF failure hazard, since the increased impoundment may increase the overall dead weight supported by the TSF dam, cause dam overtopping or encourage dam seepage, when a piping effect is induced.

5.3 | Climate change and future outlook

This work showed that large topographic change, and specifically channel geomorphic evolution, are affected by key factors, such as the amount of sediment released in the channel network, the type of physical phenomenon (e.g., landslides or debris-flow type) and other anthropogenic pressures, for example, TSF dams and mining (Dethier et al., 2023). Climate change is also an important factor in the evolution of landscape change and landslide occurrence in the Philippines, with consequences on the overall modification of river channels. Climate change will likely increase the frequency of occurrence and magnitude of rainfall events at a global scale (Gariano & Guzzetti, 2016), and the Philippines will be among the most affected areas (Gariano & Guzzetti, 2016). The results will be observable in a vast range of geomorphic settings, especially river planforms (East et al., 2022), with a substantial impact on the local populations (Gariano et al., 2017) and loss of life and property (East et al., 2022). This paper shows that an integrated modelling of the geomorphic response of the landscape to large rainfall events and (consequently) sediment release is crucial to understand the impact on river channels, which will become a much more common occurrence in a warming climate. As a result, our approach could be used as a practical tool to plan, monitor and simulate the impacts of landslides for a variety of purposes (e.g., early warning systems, design of protective or mitigation measures) that are inclusive of the increased effects of climate change under several global warming scenarios (e.g., IPCC climate projections).

6 | CONCLUSIONS

This paper investigated the role of landslide sediment delivery on channel geomorphic change during an extreme flood event in a tropical catchment impacted by mining activity. The impact of Typhoon Mangkhut on the Antamok River was chosen for the large number of landslides that occurred and the presence of several mines and in-channel TSF dams. We employed a series of methods that included: (i) manual mapping of landslide inventories and channel extents, based on satellite and aerial imagery and digital elevation models; (ii) topographic analysis and stream power to assess relationships between channel change and river hydraulics and (iii) multi-phase computational modelling using the model r.avaflow to simulate the topographic change in response to landsliding and flooding.

We found no clear relationship between landslide sediment input and channel geomorphic change, with the longitudinal pattern of channel widening complicated by mining infrastructure, specifically tailing storage facilities (TSFs). We observed widening to be greatest in the areas downstream of hillslopes with the highest landslide concentration. This effect was only observed in the reaches immediately downstream of landslide sediment inputs (up to ~1,000 m), whereas further downstream the effects on the active channel were minimal. Overall, the channel geomorphic response to Typhoon Mangkhut is spatially variable and not well explained by landslide inputs, longitudinal changes in valley bottom width or unit stream power, and is complicated by TSF dams.

Well-established methods such as stream power threshold could not explain the observed pattern of channel widening, potentially due to the role of very large sediment input provided by landslides and disruption to the flow dynamics caused by TSF dams. This limitation was overcome by using a multi-phase computational model, which consistently predicted channel width when compared to manual mapping observations. Furthermore, the model revealed spatial patterns of deposition and erosion, such as the formation and removal of a small sediment dam in the river channel network during the flood event, that were otherwise difficult to observe in the post-event imagery. The model also highlighted, in agreement with the post-event observations, the role of in-channel TSF dams in affecting river geomorphic change in response to extreme events, especially in the reach in-between the two TSFs.

A sensitivity analysis carried out on the model parameters and input factors showed that results were qualitatively consistent across the range of variability that was tested, except for a single scenario when the sediment was considered friction-dependent only. Crucially, simulations also showed that conventional expectations of increased erosional and depositional processes with increasing flow discharge may not be correct. Instead, the energy associated with sediment transport becomes of primary importance, whereby multi-phase flows are better placed to represent such phenomena.

Overall, the results provide a first step toward the assessment of changes in channel width in complex tropical catchments with landslide sediment input and impoundments that disrupt landslide-channel connectivity and flood dynamics that are difficult to observe and model. This paper paves the way for further developments in using integrated techniques and numerical models that can aid in understanding and explaining the complex interactions between landslides and rivers.

AUTHOR CONTRIBUTIONS

Diego Panici (c,d,f,h,i), Georgina Bennett (a,b,c,d,g,h,i), Richard Boothroyd (c,d,e,f,h,i), Clàudia Abancó (c,d,e,h,i), Richard Williams (a,b,c,g,h,i), Fibor Tan (a,b,d,e,i), Mark Matera (c,d,e).

Where: (a) conceptualisation; (b) funding acquisition; (c) methodology (including methodological development); (d) investigation (e.g. data collection); (e) resources (provision of data etc); (f) software (its provision and development); (g) supervision; (h) writing – initial draft; and (i) writing – reviewing and editing.

ACKNOWLEDGEMENTS

The authors are grateful to Mr Craig MacDonell for his support with the production and editing of figures in the manuscript. This investigation was jointly funded by DOST-PCIEERD and the Natural Environment Research Council (NERC) Newton Agham for the South East Asia grants NE/S003312 and NE/S003371. Richard Williams is also grateful for GCRF and Newton Fund Consolidation Account (GNCA) EP/X527749/1 and NERC grant NE/W006871/1.

DATA AVAILABILITY STATEMENT

The mapping and model results inclusive of topographic changes to the pre-event DEM are available through the NERC Environmental

Information Data Centre (EIDC) repository at https://data-package.ceh.ac.uk/data/5d17ff4b-fc98-47e5-9d61-956b17254681. GPM IMERG data are available in Google Earth Engine – https://developers.google.com/earth-engine/datasets/catalog/NASA_GPM_L3_IMERG_V06.

ORCID

Diego Panici https://orcid.org/0000-0001-7394-7981
Georgina L. Bennett https://orcid.org/0000-0002-4812-8180
Richard J. Boothroyd https://orcid.org/0000-0001-9742-4229
Clàudia Abancó https://orcid.org/0000-0002-2169-5409
Richard D. Williams https://orcid.org/0000-0001-6067-1947

REFERENCES

Abancó, C., Bennett, G., Matthews, A., Matera, M. & Tan, F. (2021) The role of geomorphology, rainfall and soil moisture in the occurrence of landslides triggered by 2018 typhoon Mangkhut in the Philippines. *Natural Hazards and Earth System Sciences*, 21(5), 1531–1550. Available from: https://doi.org/10.5194/nhess-21-1531-2021

Arattano, M. & Marchi, L. (2005) Measurements of debris flow velocity through cross-correlation of in instrumentation data. *Natural Hazards and Earth System Sciences*, 5(1), 137–142. Available from: https://doi.org/10.5194/nhess-5-137-2005

Atkinson, E. (1995) Methods for assessing sediment delivery in river systems. *Hydrological Sciences-Journal-des Sciences Hydrologiques*, 40(2), 273–280. Available from: https://doi.org/10.1080/02626669509491409

Baggio, T., Mergili, M. & D'Agostino, V. (2021) Advances in the simulation of debris flow erosion: the case study of the Rio Gere (Italy) event of the 4th august 2017. *Geomorphology*, 381, 107664. Available from: https://doi.org/10.1016/j.geomorph.2021.107664

Barman, B., Kumar, B. & Kumar Sarma, A. (2018) Turbulent flow structures and geomorphic characteristics of a mining affected Alluvial Channel: turbulence in mining affected Alluvial Channel'. *Earth Surface Processes and Landforms*, 43(9), 1811–1824. Available from: https://doi.org/10.1002/esp.4355

Benda, L. & Dunne, T. (1997) Stochastic forcing of sediment supply to channel networks from landsliding and debris flow. *Water Resources Research*, 33(12), 2849–2863. Available from: https://doi.org/10.1029/97WR02388

Bennett, G.L., Kean, J., Rengers, F., Ryan, S. & Rathburn, S. (2017) Landslide-channel feedbacks amplify flood response and channel erosion. In: *EGU general assembly 2017*, Vol. 19. Vienna: EGU, EGU2017-14326-3.

Bennett, G.L., Miller, S.R., Roering, J.J. & Schmidt, D.A. (2016) Landslides, threshold slopes, and the survival of relict terrain in the wake of the Mendocino triple junction. *Geology*, 44(5), 363–366. Available from: https://doi.org/10.1130/G37530.1

Bennett, G.L., Panici, D., Rengers, F., Kean, J. & Rathburn, S. (under review) landslide-channel feedbacks amplify channel widening. *Nature Natural Hazards*.

Bennett, G.L., Panici, D., Rengers, F., Kean, J. & Rathburn, S. (2024) Landslide-channel feedbacks amplify channel widening during floods. https://doi.org/10.21203/rs.3.rs-3937459/v1

Bizzi, S. & Lerner, D.N. (2015) The use of stream power as an indicator of channel sensitivity to erosion and deposition processes. *River Research and Applications*, 31(1), 16–27. Available from: https://doi.org/10.1002/rra.2717

Boothroyd, R.J., Williams, R.D., Hoey, T.B., MacDonell, C., Tolentino, P.L.M., Quick, L., et al. (2023) National-scale geodatabase of catchment characteristics in the Philippines for river management applications. *PLoS ONE*, 18(3), e0281933. Available from: https://doi.org/10.1371/journal.pone.0281933

Boothroyd, R.J., Williams, R.D., Hoey, T.B., Tolentino, P.L.M. & Yang, X. (2021) National-scale assessment of decadal river migration at critical bridge infrastructure in the Philippines. *Science of the Total Environment*, 768, 144460. Available from: https://doi.org/10.1016/j.scitotenv.2020.144460

Bureau of Soils and Water Management (BSWM). (2012), *Soil type map*. Manila: Bureau of Soils and Water Manage, available at: https://www.geoportal.gov.ph/ (last access: 10 February 2023).

Carating, R.B., Galanta, R.G. & Bacatio, C.D. (2014) *The soils of the Philippines*. Netherlands, Dordrecht: Springer.

Catane, S.G., Abon, C.C., Saturay, R.M., Mendoza, E.P.P. & Futalan, K.M. (2012) Landslide-amplified flash floods-the June 2008 Panay Island flooding, Philippines. *Geomorphology*, 169–170(June 2008), 55–63. Available from: https://doi.org/10.1016/j.geomorph.2012.04.008

Catto, J.L. & Dowdy, A. (2021) Understanding compound hazards from a weather system perspective. *Weather and Climate Extremes*, 32(May 2020), 100313. Available from: https://doi.org/10.1016/j.wace.2021.100313

Chen, H.X., Zhang, L.M., Gao, L., Yuan, Q., Lu, T., Xiang, B., et al. (2017) Simulation of interactions among multiple debris flows. *Landslides*, 14(2), 595–615. Available from: https://doi.org/10.1007/s10346-016-0710-x

Church, M. (2006) Bed material transport and the morphology of alluvial river channels. *Annual Review of Earth and Planetary Sciences*, 34(1), 325–354. Available from: https://doi.org/10.1146/annurev.earth.33.092203.122721

Clubb, F.J., Weir, E.F. & Mudd, S.M. (2022) Continuous measurements of valley floor width in mountainous landscapes. *Earth Surface Dynamics*, 10(3), 437–456. Available from: https://doi.org/10.5194/esurf-10-437-2022

Collins, B. & Sheikh, A. (2004) *Historical Channel locations of the Nooksack River*. Bellingham, Washington, US: Whatcom County Public Works Department.

Corpus, T.J., David, C.P., Murao, S. & Maglambayan, V. (2011) Smallscale gold Mining in the Ambalanga Catchment, Philippines: its control on mercury methylation in stream sediments. *International Journal of Environmental Sciences*, 2(2), 1048–1059.

Cox, J.R., Huismans, Y., Knaake, S.M., Leuven, J.R.F.W.N., Vellinga, E., Vegt, M., et al. (2021) Anthropogenic effects on the contemporary sediment budget of the lower Rhine-Meuse Delta channel network. *Earth's Future*, 9(7), Available from: https://doi.org/10.1029/2020EF001869

Croissant, T., Lague, D., Steer, P. & Davy, P. (2017) Rapid post-seismic landslide evacuation boosted by dynamic river width. *Nature Geoscience*, 10(9), 680–684. Available from: https://doi.org/10.1038/ngeo3005

Dabiri, Z., Hölbling, D., Abad, L., Helgason, J. K., Sæmundsson, Þ. & Tiede, D. (2020) Assessment of Landslide-Induced Geomorphological Changes in Hítardalur Valley, Iceland, Using Sentinel-1 and Sentinel-2 Data. *Applied Sciences*, 10(17), 5848. https://doi.org/10.3390/app10175848

DeLisle, C., Yanites, B.J., Chen, C.Y., Shyu, J.B.H. & Rittenour, T.M. (2021) Extreme event-driven sediment aggradation and erosional buffering along a tectonic gradient in southern Taiwan. *Geology*, 50(1), 16–20. Available from: https://doi.org/10.1130/G49304.1

Dethier, E.N., Silman, M., Leiva, J.D., Alqahtani, S., Fernandex, L.E., Pauca, P., et al. (2023) A global rise in alluvial mining increases sediment load in tropical rivers. *Nature*, 620(7975), 787–793. Available from: https://doi.org/10.1038/s41586-023-06309-9

Dingle, E.H., Paringit, E.C., Tolentino, P.L.M., Williams, R.D., Hoey, T.B., Barrett, B., et al. (2019) Decadal-scale morphological adjustment of a lowland Tropical River. *Geomorphology*, 333, 30–42. Available from: https://doi.org/10.1016/j.geomorph.2019.01.022

Donovan, M., Belmont, P., Notebaert, B., Coombs, T., Larson, P. & Souffront, M. (2019) Accounting for uncertainty in remotely-sensed measurements of river planform change. *Earth-Science Reviews*, 193, 220–236. Available from: https://doi.org/10.1016/j.earscirev.2019.04.009

East, A.E., Jenkins, K.J., Happe, P.J., Bountry, J.A., Beechie, T.J., Mastin, M.C., et al. (2017) Channel-planform evolution in four rivers of Olympic National Park, Washington, USA: the roles of physical drivers and trophic cascades. *Earth Surface Processes and Landforms*, 42(7), 1011–1032. Available from: https://doi.org/10.1002/esp.4048

East, A.E., Logan, J.B., Mastin, M.C., Ritchie, A.C., Bountry, J.A., Magirl, C.S., et al. (2018) Geomorphic evolution of a gravel-bed river under sediment-starved versus sediment-rich conditions:

river response to the world's largest dam removal. *Journal of Geophysical Research: Earth Surface*, 123(12), 3338–3369. Available from: https://doi.org/10.1029/2018JF004703

East, A.E., Warrick, J.A., Li, D., Sankey, J.B., Redsteer, M.H., Gibbs, A.E., et al. (2022) Measuring and attributing sedimentary and geomorphic responses to modern climate change: challenges and opportunities. *Earth's Future*, 10(10), Available from: https://doi.org/10.1029/2022ef002983

Ehasz, J.L., Bureau, G.J., Babbitt, D., Barneich, J.A., Beikae, M., Ghanaat, Y., et al. (1992) *Observed performance of dams during earthquakes*. U.S.: Committee on Large Dams.

Emberson, R., Kirschbaum, D., Amatya, P., Tanyas, H. & Marc, O. (2022) Insights from the topographic characteristics of a large global catalog of rainfall-induced landslide event inventories. *Natural Hazards and Earth System Sciences Discussions*, 22(3), 1129–1149. Available from: https://doi.org/10.5194/nhess-2021-250

Ferencevic, M.V. & Ashmore, P. (2012) Creating and evaluating digital elevation model-based stream-power map as a stream assessment tool. *River Research and Applications*, 28(9), 1394–1416. Available from: https://doi.org/10.1002/rra.1523

Ferguson, R.I., Church, M., Rennie, C.D. & Venditti, J.G. (2015) Reconstructing a sediment pulse: modeling the effect of placer mining on Fraser River, Canada. *Journal of Geophysical Research: Earth Surface*, 120(7), 1436–1454. Available from: https://doi.org/10.1002/2015jf003491

Froude, M.J. & Petley, D.N. (2018) Global fatal landslide occurrence from 2004 to 2016. *Natural Hazards and Earth System Sciences*, 18(8), 2161–2181. Available from: https://doi.org/10.5194/nhess-18-2161-2018

Fryirs, K.A., Wheaton, J.M. & Brierley, G.J. (2016) An approach for measuring confinement and assessing the influence of valley setting on river forms and processes. *Earth Surface Processes and Landforms*, 41(5), 701–710. Available from: https://doi.org/10.1002/esp.3893

Gariano, S.L. & Guzzetti, F. (2016) Landslides in a changing climate. *Earth-Science Reviews*, 162, 227–252. Available from: https://doi.org/10.1016/j.earscirev.2016.08.011

Gariano, S.L., Rianna, G., Petrucci, O. & Guzzetti, F. (2017) Assessing future changes in the occurrence of rainfall-induced landslides at a regional scale. *Science of the Total Environment*, 596–597, 417–426. Available from: https://doi.org/10.1016/j.scitotenv.2017.03.103

Geertsema, M., Menounos, B., Bullard, G., Carrivick, J.L., Clague, J.J., Dai, C., et al. (2022) The 28 November 2020 landslide, tsunami, and outburst flood – a hazard cascade associated with rapid deglaciation at Elliot Creek, British Columbia, Canada. *Geophysical Research Letters*, 49(6), e2021GL096716. Available from: https://doi.org/10.1029/2021GL096716

Golly, A. & Turowski, J.M. (2017) Deriving principal channel metrics from bank and long-profile geometry with the R package cmgo. *Earth Surface Dynamics*, 5(3), 557–570. Available from: https://doi.org/10.5194/esurf-5-557-2017

Grafil, L. & Castro, O. (2014) Acquisition of IfSAR for the production of nationwide DEM and ORI for the Philippines under the unified mapping project. *Info*, 21, 12-13 and 40-43.

Gran, K.B., Montgomery, D.R. & Halbur, J.C. (2011) Long-term elevated post-eruption sedimentation at mount Pinatubo, Philippines. *Geology*, 39(4), 367–370. Available from: https://doi.org/10.1130/G31682.1

Guzzetti, F., Ardizzone, F., Cardinali, M., Rossi, M. & Valigi, D. (2009) Landslide volumes and landslide mobilization rates in Umbria, Central Italy. *Earth and Planetary Science Letters*, 279(3–4), 222–229. Available from: https://doi.org/10.1016/j.epsl.2009.01.005

Henshaw, A.J., Sekarsari, P.W., Zolezzi, G. & Gurnell, A.M. (2020) Google earth as a data source for investigating river forms and processes: discriminating river types using form-based process indicators. *Earth Surface Processes and Landforms*, 45(2), 331–344. Available from: https://doi.org/10.1002/esp.4732

Holden, W.N. & Jacobson, D.R. (2012) *Mining and natural Hazard vulnerability in the Philippines: digging to development or digging to disaster?* London: Anthem Press.

Huffman, G.J., Stocker, E.F., Bolvin, D.T., Nelkin, E.J. & Tan, J. (2019) *GPM IMERG final precipitation L3 half hourly 0.1 degree _ 0.1 degree V06*. Greenbelt, MD: Goddard Earth Sciences Data and Information Services Center.

Iverson, R.M. (2000) Landslide triggering by rain infiltration. *Water Resources Research*, 36(7), 1897–1910. Available from: https://doi.org/10.1029/2000WR900090

Iverson, R.M., Reid, M.E. & LaHusen, R.G. (1997) Debris-flow mobilization from landslides. *Annual Review of Earth and Planetary Sciences*, 25(1), 85–138. Available from: https://doi.org/10.1146/annurev.earth.25.1.85

Jain, V., Preston, N., Fryirs, K.A. & Brierley, G.J. (2006) Comparative assessment of three approaches for deriving stream power plots along long profiles in the upper Hunter River catchment, New South Wales, Australia. *Geomorphology*, 74(1-4), 297–317. Available from: https://doi.org/10.1016/j.geomorph.2005.08.012

James, L.A. (2013) Legacy sediment: definitions and processes of episodically produced anthropogenic sediment. *Anthropocene*, 2, 16–26. Available from: https://doi.org/10.1016/j.ancene.2013.04.001

Jayawardena, A., Takeuchi, K. & Machbub, B. (1997) Ilog Itaas ng Agno. In: *CATALOGUE OF RIVERS FOR SOUTHEAST ASIA AND THE PACIFIC-volume II*. Bangkok, Thailand: UNESCO, p. 285.

Keck, J., Istanbulluoglu, E., Lundquist, J., Bandaragoda, C., Jaeger, K., Mauger, G., et al. (2022) How does precipitation variability control bedload response across a mountainous channel network in a maritime climate? *Water Resources Research*, 58(8), e2021WR030358. Available from: https://doi.org/10.1029/2021WR030358

Khan, S. & Fryirs, K.A. (2020) Application of globally available, coarse-resolution digital elevation models for delineating valley bottom segments of varying length across a catchment. *Earth Surface Processes and Landforms*, 45(12), 2788–2803. Available from: https://doi.org/10.1002/esp.4930

Kirschbaum, D. & Stanley, T. (2018) Satellite-based assessment of rainfall-triggered landslide Hazard for situational awareness. *Earth's Future*, 6(3), 505–523. Available from: https://doi.org/10.1002/2017EF000715

Kirschbaum, D., Stanley, T. & Zhou, Y. (2015) Spatial and temporal analysis of a global landslide catalog. *Geomorphology*, 249, 4–15. Available from: https://doi.org/10.1016/j.geomorph.2015.03.016

Kirschbaum, D., Watson, C.S., Rounce, D.R., Shugar, D.H., Kargel, J.S., Haritashya, U.K., et al. (2019) The state of remote sensing capabilities of cascading hazards over High Mountain Asia. *Frontiers in Earth Science*, 7, Available from: https://doi.org/10.3389/feart.2019.00197

Kondolf, G.M. (1997) Hungry water: effects of dams and gravel mining on river channels. *Environmental Management*, 21(4), 533–551. Available from: https://doi.org/10.1007/s002679900048

Korup, O. (2005) Geomorphic imprint of landslides on alpine river systems, Southwest New Zealand. *Earth Surface Processes and Landforms*, 30(7), 783–800. Available from: https://doi.org/10.1002/esp.1171

Korup, O., Densmore, A.L. & Schlunegger, F. (2010) The role of landslides in mountain range evolution. *Geomorphology*, 120(1–2), 77–90. Available from: https://doi.org/10.1016/j.geomorph.2009.09.017

Kumar, V., Gupta, V., Jamir, I. & Chattoraj, S.L. (2019) Evaluation of potential landslide damming: case study of Urni landslide, Kinnaur, Satluj valley, India. *Geoscience Frontiers*, 10(2), 753–767. Available from: https://doi.org/10.1016/j.gsf.2018.05.004

LaHusen, S.R., Duvall, A.R., Booth, A.M., Grant, A., Mishkin, B.A., Montgomery, D.R., et al. (2020) Rainfall triggers more deep-seated landslides than Cascadia earthquakes in the Oregon coast range, USA. *Science Advances*, 6(38), Available from: https://doi.org/10.1126/sciadv.aba6790

Larsen, I.J., Montgomery, D.R. & Korup, O. (2010) Landslide erosion controlled by hillslope material. *Nature Geoscience*, 3(4), 247–251. Available from: https://doi.org/10.1038/ngeo776

Macasieb, R.Q., Orozco, C.R. & Resurreccion, A.C. (2021a) Heavy metal contamination assessment and source apportionment analysis using multivariate methods in surface sediments of mining-impacted rivers in Benguet. *International Journal of Environmental Studies*, 78(2), 283–300. Available from: https://doi.org/10.1080/00207233.2020.1802953

Macasieb, R.Q., Orozco, C.R. & Resurreccion, A.C. (2021b) Application of coupled HEC-HMS and US EPA WASP for transport modelling of mercury in the mining-impacted Ambalanga River. *ASEAN Engineering Journal*, 11(3), 158–176. Available from: https://doi.org/10.11113/aej.v11.17052

Magilligan, F.J., Buraas, E.M. & Renshaw, C.E. (2015) The efficacy of stream power and flow duration on geomorphic responses to catastrophic flooding. *Geomorphology*, 228, 178–188. Available from: https://doi.org/10.1016/j.geomorph.2014.08.016

Mandarino, A., Pepe, G., Maerker, M., Cevasco, A. & Brandolini, P. (2020) Short-term GIS analysis for the assessment of the recent active-channel planform adjustments in a widening, highly altered river: the Scrivia River, Italy. *Watermark*, 12(2), 514. Available from: https://doi.org/10.3390/w12020514

Mergili, M., Jaboyedoff, M., Pullarello, J. & Pudasaini, S.P. (2020) Back calculation of the 2017 Piz Cengalo–Bondo landslide cascade with r.avaflow: what we can do and what we can learn. *Natural Hazards and Earth System Sciences*, 20, 505–520. Available from: https://doi.org/10.5194/nhess-20-505-2020

Mergili, M., Pudasaini, S.P., Emmer, A., Fischer, J., Cochachin, A. & Frey, H. (2020) Reconstruction of the 1941 GLOF process chain at Lake Palcacocha (cordillera Blanca, Peru). *Hydrology and Earth System Sciences*, 24(1), 93–114. Available from: https://doi.org/10.5194/hess-24-93-2020

National Disaster Risk Reduction and Management Center. (2018). *Preparedness measures and effects for typhoon "OMPONG"* (I.N. "MANGKHUT") (SitRep No. 48, 133 pages). Quezon City: National Disaster Risk Reduction and Management Council. http://ndrrmc.gov.ph/attachments/article/3437/SitRep_No_48_re_Preparedness_Measures_and_Effects_for_Typhoon_OMPONG_IN_MANGKHUT_as_of_6PM_28_Sept_2018_to_6AM_29_Sept_2018.pdf (accessed on 16/06/2023)

Nelson, A. & Dubé, K. (2016) Channel response to an extreme flood and sediment pulse in a mixed bedrock and gravel-bed river. *Earth Surface Processes and Landforms*, 41(2), 178–195. Available from: https://doi.org/10.1002/esp.3843

Nones, M. (2019) Dealing with sediment transport in flood risk management. *Acta Geophysica*, 67(2), 677–685. Available from: https://doi.org/10.1007/s11600-019-00273-7

Ocampo, L.A. & Schmitz, S. (2023) Accumulation by dispossession and hazardscape production in post-corporate gold mining in Itogon, Philippines. *Geographical Research*, 61(1), 44–57. Available from: https://doi.org/10.1111/1745-5871.12565

Palangdan, V.T. (2018) *Save, recovery and development of Itogon. A rehabilitation and recovery plan of the municipality of Itogon, Benguet (2019–2028)*, Vol. 2018. Itogon, Philippines, 54 pp.: Itogon Local Government Unit.

Paliaga, G., Faccini, F., Luino, F., Turconi, L. & Bobrowsky, P. (2019) Geomorphic processes and risk related to a large landslide dam in a highly urbanized Mediterranean catchment (Genova, Italy). *Geomorphology*, 327, 48–61. Available from: https://doi.org/10.1016/j.geomorph.2018.10.020

Parker, C. & Davey, J. (2023) Stream power indices correspond poorly with observations of alluvial river channel adjustment. *Earth Surface Processes and Landforms*, 48(6), 1290–1304. Available from: https://doi.org/10.1002/esp.5550

Pudasaini, S.P. & Mergili, M. (2019) A multi-phase mass flow model. *Journal of Geophysical Research: Earth Surface*, 124(12), 2920–2942. Available from: https://doi.org/10.1029/2019JF005204

Rachelly, C., Vetsch, D.F., Boes, R.M. & Weitbrecht, V. (2022) Sediment supply control on morphodynamic processes in gravel-bed river widenings. *Earth Surface Processes and Landforms*, 47(15), 3415–3434. Available from: https://doi.org/10.1002/esp.5460

Rinaldi, M., Wyzga, B. & Surian, N. (2005) Sediment mining in alluvial channels: physical effects and management perspectives. *River Research and Applications*, 21(7), 805–828. Available from: https://doi.org/10.1002/rra.884

Schlunegger, F., Badoux, A., McArdell, B.W., Gwerder, C., Schnydrig, D., Rieke-Zapp, D., et al. (2009) Limits of sediment transfer in an alpine debris-flow catchment, Illgraben, Switzerland. *Quaternary Science Reviews*, 28(11–12), 1097–1105. Available from: https://doi.org/10.1016/j.quascirev.2008.10.025

Schwanghart, W. & Scherler, D. (2014) TopoToolbox 2 – MATLAB-based software for topographic analysis and modeling in earth surface sciences. *Earth Surface Dynamics*, 2(1), 1–7. Available from: https://doi.org/10.5194/esurf-2-1-2014

Schwanghart, W. & Scherler, D. (2017) Bumps in river profiles: uncertainty assessment and smoothing using quantile regression techniques. *Earth Surface Dynamics*, 5(4), 821–839. Available from: https://doi.org/10.5194/esurf-5-821-2017

Sholtes, J.S., Yochum, S.E., Scott, J.A. & Bledsoe, B.P. (2018) Longitudinal variability of geomorphic response to floods. *Earth Surface Processes and Landforms*, 43(15), 3099–3113. Available from: https://doi.org/10.1002/esp.4472

Shugar, D.H., Jacquemart, M., Shean, D., Bhushan, S., Upadhyay, K., Sattar, A., et al. (2021) A massive rock, ice avalanche caused the 2021 disaster at Chamoli, Indian Himalaya. *Science*, 373(6552), 300–306. Available from: https://doi.org/10.1126/science.abh4455

Slater, L.J. (2016) To what extent have changes in channel capacity contributed to flood hazard trends in England and Wales? *Earth Surface Processes and Landforms*, 41(8), 1115–1128. Available from: https://doi.org/10.1002/esp.3927

Slater, L.J., Singer, M.B. & Kirchner, J.W. (2015) Hydrologic versus geomorphic drivers of trends in flood hazard. *Geophysical Research Letters*, 42(2), 370–376. Available from: https://doi.org/10.1002/2014GL062482

Stephenson, V., Finlayson, A. & Morel, L.M. (2018) A risk-based approach to shelter resilience following flood and typhoon damage in rural Philippines. *Geosciences*, 8(2), 76. Available from: https://doi.org/10.3390/geosciences8020076

Suwa, H., Okano, K. & Kanno, T. (2009) Behavior of debris flows monitored on test slopes of Kamikamihorizawa Creek, mount Yakedake, Japan. *International Journal of Erosion Control Engineering*, 2(2), 33–45. Available from: https://doi.org/10.13101/ijece.2.33

Tabios III, G.Q. (2020) *Reservoir sedimentation studies*. Cham: Springer, pp. 165–209.

Tarolli, P. & Sofia, G. (2016) Human topographic signatures and derived geomorphic processes across landscapes. *Geomorphology*, 255, 140–161. Available from: https://doi.org/10.1016/j.geomorph.2015.12.007

Tolentino, P.L.M., Poortinga, A., Kanamaru, H., Keesstra, S., Maroulis, J., David, C.P.C., et al. (2016) Projected impact of climate change on hydrological regimes in the Philippines. *PLoS ONE*, 11(10), e0163941. Available from: https://doi.org/10.1371/journal.pone.0163941

Tseng, C.M., Lin, C.W., Dalla Fontana, G. & Tarolli, P. (2015) The topographic signature of a major typhoon. *Earth Surface Processes and Landforms*, 40(8), 1129–1136. Available from: https://doi.org/10.1002/esp.3708

Wang, T., Huang, T., Shen, P., Peng, D. & Zhang, L. (2023) The mechanisms of high mobility of a glacial debris flow using the Pudasaini-Mergili multi-phase modeling. *Engineering Geology*, 322, 107186. Available from: https://doi.org/10.1016/j.enggeo.2023.107186

Wang, Y., Hutter, K. & Pudasaini, S. (2004) The savage-Hutter theory: a system of partial differential equations for avalanche flows of snow, debris, and mud. *Journal of Applied Mathematics and Mechanics*, 84(8), 507–527. Available from: https://doi.org/10.1002/zamm.200310123

Weather Division PAGASA. (2018) *Summary report typhoon Ompong (Mangkhut/1822)*. Quezon City, Philippines: PAGASA. available at: https://pubfiles.pagasa.dost.gov.ph/pagasaweb/files/tamss/weather/tcsummary/TY_Ompong_Mangkhut.pdf (last access: 10 February 2023),

Winterbottom, S.J. (2000) Medium and short-term channel planform changes on the Rivers Tay and Tummel, Scotland. *Geomorphology*, 34(3-4), 195–208. Available from: https://doi.org/10.1016/S0169-555X(00)00007-6

Wistuba, M., Malik, I., Wójcicki, K. & Michałowicz, P. (2015) Coupling between landslides and eroding stream channels reconstructed from spruce tree rings (examples from the Carpathians and Sudetes -

Central Europe). *Earth Surface Processes and Landforms*, 40(3), 293–312. Available from: https://doi.org/10.1002/esp.3632

Wobus, C., Whipple, K.X., Kirby, E., Snyder, N., Johnson, J., Spyropolou, K., et al. (2006) Tectonics from topography: procedures, promise, and pitfalls. *GSA Special Papers*, 398, 55–74. Available from: https://doi.org/10.1130/2006.2398(04

Wohl, E. (2015) Legacy effects on sediments in river corridors. *Earth-Science Reviews*, 147, 30–53. Available from: https://doi.org/10.1016/j.earscirev.2015.05.001

Yanites, B.J., Mitchell, N.A., Bregy, J.C., Carlson, G.A., Cataldo, K., Holahan, M., et al. (2018) Landslides control the spatial and temporal variation of channel width in southern Taiwan: implications for landscape evolution and cascading hazards in steep, tectonically active landscapes. *Earth Surface Processes and Landforms*, 43(9), 1782–1797. Available from: https://doi.org/10.1002/esp.4353

Zhao, T., Dai, F. & Xu, N. (2017) Coupled DEM-CFD investigation on the formation of landslide dams in narrow rivers. *Landslides*, 14(1), 189–201. Available from: https://doi.org/10.1007/s10346-015-0675-1

How to cite this article: Panici, D., Bennett, G.L., Boothroyd, R.J., Abancó, C., Williams, R.D., Tan, F. et al. (2024) Observations and computational multi-phase modelling in tropical river settings show complex channel changes downstream from rainfall-triggered landslides. *Earth Surface Processes and Landforms*, 1–19. Available from: https://doi.org/10.1002/esp.5841